Superphénix Benchmark Part I: Results of Static neutronics

Ponomarev, A.; Mikityuk, K.; Zhang, L.; Nikitin, E.; Fridman, E.; Álvarez-Velarde, F.; Romojaro-Otero, P.; Jiménez-Carrascosa, A.; García-Herranz, N.; Lindley, B.; Davies, U.; Seubert, A.; Henry, R.;

Originally published:

June 2021

Journal of Nuclear Engineering and Radiation Science 8(2022)1, 011320

DOI: https://doi.org/10.1115/1.4051449

Perma-Link to Publication Repository of HZDR:

https://www.hzdr.de/publications/Publ-32426

SPX Benchmark Part I: Results of Static Neutronics

Alexander Ponomarev[1]

Paul Scherrer Institute (PSI)

Forschungsstrasse 111, 5232 Villigen PSI, Schweiz.PSI

alexander.ponomarev@psi.ch

Konstantin Mikityuk

Paul Scherrer Institute (PSI)

Forschungsstrasse 111, 5232 Villigen PSI, Schweiz.PSI

konstantin.mikityuk@psi.ch

Liang Zhang

Paul Scherrer Institute (PSI)

Forschungsstrasse 111, 5232 Villigen PSI, Schweiz.PSI

liang.zhang@psi.ch

Evgeny Nikitin

Helmholtz-Zentrum Dresden-Rossendorf (HZDR)

Bautzner Landstraße 400, DE-01328 Dresden, Germany

e.nikitin@hzdr.de

Emil Fridman

Helmholtz-Zentrum Dresden-Rossendorf (HZDR)

[1] Corresponding author

Bautzner Landstraße 400, DE-01328 Dresden, Germany

e.fridman@hzdr.de

Francisco Álvarez-Velarde

Centro de Investigaciones Energéticas, MedioAmbientales y Tecnológicas (CIEMAT)

Avda. Complutense, 40. 28040, Madrid, Spain

francisco.alvarez@ciemat.es

Pablo Romojaro Otero

Centro de Investigaciones Energéticas, MedioAmbientales y Tecnológicas (CIEMAT) – Currently at SCK·CEN

Avda. Complutense, 40. 28040, Madrid, Spain

pablo.romojaro@sckcen.be

Antonio Jiménez-Carrascosa

Universidad Politécnica de Madrid (UPM)

José Gutiérrez Abascal, 2, 28006, Madrid, Spain

antonio.jcarrascosa@upm.es

Nuria García-Herranz

Universidad Politécnica de Madrid (UPM)

José Gutiérrez Abascal, 2, 28006, Madrid, Spain

nuria.garcia.herranz@upm.es

Ben Lindley

University of Wisconsin-Madison

Engineering Research Building, 1500 Engineering Drive, Madison, WI53706, USA

lindley2@wisc.edu

Una Baker

University of Cambridge

Department of Engineering, Trumpington Street, Cambridge - CB2 1PZ, United Kingdom

ud215@cam.ac.uk

Armin Seubert

Gesellschaft für Anlagen- und Reaktorsicherheit (GRS) gGmbH

Boltzmannstraße 14, 85748 Garching bei München, Germany

armin.seubert@grs.de

Romain Henry

Gesellschaft für Anlagen- und Reaktorsicherheit (GRS) gGmbH

Boltzmannstraße 14, 85748 Garching bei München, Germany

romain.henry@grs.de

ABSTRACT

In the paper, the specification of a new neutronics benchmark for a large Sodium cooled Fast Reactor (SFR) core and results of modelling by different participants are presented. The neutronics benchmark describes the core of the French sodium cooled reactor Superphénix at its start-up configuration, which in particular was used for experimental measurement of reactivity characteristics. The benchmark consists of the detailed heterogeneous core specification for neutronic analysis and results of the reference solution. Different core geometries and thermal conditions from cold "as fabricated" up to full power were considered. The reference Monte Carlo (MC) solution of Serpent 2 includes data on multiplication factor, power distribution, axial and radial reaction rates distribution, reactivity coefficients and safety characteristics, control rods worth, kinetic data. The results of modelling with seven other solutions using deterministic and MC methods are also presented and compared to the reference solution. The comparisons results demonstrate appropriate agreement of evaluated characteristics. The neutronics results will be used in the second phase of the benchmark for evaluation of transient behaviour of the core.

1. INTRODUCTION

The paper presents a new neutronics benchmark for a large Sodium cooled Fast Reactor (SFR) core and results of modelling by different participants. Number of detailed neutronics benchmarks for fast reactor cores is rather limited. Decrease of the interest to these reactors is observed as to ones not demanded in the nearest future. Nonetheless, the actuality of the proposed new benchmark is evident. It is a new benchmark with detailed heterogeneous core description and definition of different core reactivity configurations. With fast development of neutronics tools (codes) supported by an outstanding development of fast computing technics, an accurate treatment of the detailed heterogeneous geometries with nearly all core structural elements in solving neutron transport using Monte Carlo (MC) or modern deterministic is becoming more common. Furthermore the new benchmark uses advantages of the available experimental data, being constructed on the basis of pre-existing reactor core and keeping its neutronics characteristics. In addition, the benchmark was essentially actual for cross validation of the tools used in the ESFR-SMART project [1] for evaluation of neutronic characteristics of the new SFR core with low sodium void effect.

The neutronics benchmark describes the core of the French SFR Superphénix (SPX). It contains the detailed core specification for neutronic analysis and results of the reference solution, as well as results obtained with seven other solutions. It is based on the core arrangement as has been achieved during start-up tests of the reactor [2]. The Superphénix reactor employs the core of a conventional type SFR that comprises the fissile MOX fuel subassemblies with two different fissile isotopes content and outer breeder zone with fertile uranium oxide fuel subassemblies. The subassemblies are arranged in triangular lattice and composed of the pin bundle and bearing it hexagonal wrapper (hexcan). The fissile subassemblies incorporate also lower and upper axial breeder zones with fertile uranium oxide pellets, realised within the same fuel pin.

The paper is structured as following. After given introduction (Chapter 1) and overview of the core characteristics (Chapter 2), the Chapter 3 provides the detailed core specification data for neutronics modelling. The Chapter 4 contains description of expected core characteristics and parameters proposed to be evaluated within the benchmark with given definitions and the results of the reference solution using the Monte Carlo (MC) Serpent 2 code [3] with the JEFF-3.1.1 neutron cross section library [4]. The Section 5 provides the description of tools and results of modelling using seven other solutions and comparisons. Conclusions are given in last Section.

2. GENERAL PARAMETERS OF THE SUPERPHENIX REACTOR CORE

Table 1 provides the general data on Superphénix reactor core and its nominal operating conditions [2]. The core has been designed for a large commercial size breeder reactor with thermal power of 3000 MW.

3. NEUTRONICS BENCHMARK SPECIFICATION

3.1. Core model overview

The Benchmark core model is based on Superphénix start-up core layout which has been simplified for the benchmark purposes by eliminating the three neutron guide subassemblies [2]. The radial layout of the model comprises the subassemblies up to the ones of the second raw of radial steel shielding. Axially the model represents the subassembly structure from the bottom of the fissile fuel pin to the upper subassembly end which is top of the subassembly outlet shielding sleeve. The model assumes detailed heterogeneous description of most of structures including geometry of the fuel pin, subassembly wrapper, inlet and outlet sections as well as description of absorber rods.

3.2. Radial core layout

The core model radial layout is presented in Figure 1. The core model is composed of 190 inner fissile core (IC) subassemblies (SAs), 168 outer fissile core (OC) SAs, 225 radial breeder blanket (RB) SAs, 18 steel diluent SAs, 21 control and shutdown rods (CSD), three diverse shutdown rods (DSD) and 294 steel radial reflector SAs. The distribution of SAs throughout the core is given in Figure 1.

Core radial dimension is defined by SA pitch parameter, which is calculated in accord with core thermal state. The outer core boundary is defined as boundary with vacuum.

3.3. Axial core layout

The axial layout of SAs of different type is presented in Figure 2. All CSD and DSD absorber rods are shown located at their parking position. Total axial height of the model is defined in accord with the thermal core state. The axial segment heights are also given in the Figure 2 which are calculated in accord with material thermal expansion data and assumptions on core elements expansion.

The zones with detailed geometry are marked as HET in Figure 2. The HET zones of the model consider accurate subassembly geometry (namely the elements of hexagonal wrapper (hexcan), pin bundle, outlet sleeve, etc.) arranged in the diagrid with the given pitch and surrounded with sodium outside the hexcan. Some zones marked as HOM are represented by homogenized material mixture corresponding to the subassembly cell in the diagrid with dimension of SA pitch.

3.4. Radial layout of subassemblies

3.4.1. Fissile subassembly

The fissile subassembly contains 271 pins distanced by the spacer wire wrap. The radial cross section of the pin bundle at level of fissile fuel pellet is presented in Figure 3. The data on radial dimensions of the SA and pin is collected in Table 2 (the corresponding core states are described in detail below in Section 3.6). The fissile pellets are hollow ones, while the fertile pellets are solid. The outer cladding radius is evaluated accounting for the spacer wire. The upper and lower gas expansion zones constitute an empty pin cladding. The pin plug is modelled as a solid pin with the same outer diameter. The fuel pellet support axial zone in all SAs is modelled as a pin cladding with the inner hole of 5 mm in diameter. A short sodium plenum formed by transition section of subassembly between the top of the pin bundle and the outlet section is modelled as the hexcan only. The outlet section – outlet steel shielding sleeve – is modelled as a solid steel sleeve with the hexcan outer geometry and inner cylindrical channel for the main sodium flow.

3.4.2. Fertile subassembly

Fertile radial breeder subassembly contains 91 thick breeder pins. The overall axial structure of the fertile SA is similar to the fissile one. Only an additional axial region of inlet section has been introduced and is represented by the hexcan only, thus being identical to the sodium plenum above the pin bundle. The radial cross section of the pin bundle of the fertile SA with fertile fuel pellets is presented in Figure 4. The data on radial dimensions of the SA and pin is collected in Table 3.

3.4.3. Control and shutdown rods subassemblies

Control and shutdown rod subassemblies are modelled in a simplified manner assuming the absorber rod body and the empty channel (follower) as depicted in Figure 2. The absorber rod body is modelled by a bundle of 31 absorber pins (Figure 5) containing 90%-enriched boron carbide. The CSD and DSD rods differ by the length of absorber body only (160 cm and 100 cm respectively at “as fabricated” geometry). The shutdown rods position is fixed for all benchmark calculations and located at parking position at the top of upper axial blanket (Figure 2). The data on radial dimensions of the SA with absorber rod is collected in Table 4.

3.4.4. Steel radial shielding and steel diluent subassemblies

Steel radial shielding and steel diluent subassemblies are represented by three axial segments. Inlet section is modelled as hexcan only. The middle section is represented by a homogeneous mixture of construction steel and sodium different for diluent and radial shielding. The upper section is modelled as outlet sleeve which is identical to the one of fuel subassembly.

3.5. Material compositions

The material compositions used in the model are collected in Tables 5-12. There are three individual fuel compositions: the inner core fissile fuel, the outer core fissile fuel and one fertile fuel

composition for all breeder zones of the core. All steel elements are made of 316Ti construction steel. All empty volumes inside the cladding of fuel and absorber pins are filled with He-4 with isotope number density of $1 \cdot 10^{19}$ cm^{-3}.

3.6. Thermal expansion of the core and assumptions

The core model has been considered assuming a number of thermal states which differ by material temperatures and corresponding dimensions and densities. There are four thermal core states defined in the benchmark (see also Table 2):

1. "As fabricated" at 20°C.
2. "Cold" at 180°C corresponding to first achieved initial critical state.
3. "Hot Zero Power" (HZP) at 400°C corresponding to initial core uniformly heated up to inlet sodium temperature.
4. "Hot Full Power" (HFP) corresponding to nominal power conditions.

The characteristics of considered thermal states are summarized in Table 13.

There is a number of assumptions considered for the calculation of the thermal core expansion. All steel elements of the core expand axially and radially with the linear expansion coefficient of the 316Ti construction steel. The linear temperature expansion coefficient is defined as following:

$$\alpha_l(T) = 1.294 \cdot 10^{-5} + 9.354 \cdot 10^{-9} \cdot T - 3.314 \cdot 10^{-12} \cdot T^2, [1/K], \quad (1)$$

where *T* is steel temperature given in K. The steel density is corrected in accord to this expansion.

The radial expansion of the diagrid defining the subassembly pitch in the model is calculated, in accord to the core design, with use of linear expansion coefficient of 304L construction steel:

$$\alpha_l(T) = 1.216 \cdot 10^{-5} + 9.877 \cdot 10^{-9} \cdot T - 3.323 \cdot 10^{-12} \cdot T^2, [1/K], \quad (2)$$

where *T* is steel temperature given in K.

Fuel pellet stack thermal expansion is calculated independently from the cladding expansion assuming conditions with no contact and mechanical interaction between the fuel pellet and cladding for both fissile and fertile fuel types. In addition, for the calculation of fuel expansion the fuel pellet stack height is only modified in accord with linear expansion of MOX fuel, while the radial dimensions of the fuel pellet are kept as fabricated. Accordingly, the fuel density is modified. This way helped to ensure the fuel mass conservation in the model. For calculation of linear dimension change of the MOX fuel the mean linear expansion coefficients has been considered resulted in the following derivation for the dimension change:

$$\frac{L(T)}{L_0} = 9.9734 \cdot 10^{-1} + 9.802 \cdot 10^{-6} \cdot T - 2.705 \cdot 10^{-10} \cdot T^2 + 4.391 \cdot 10^{-13} \cdot T^3, T \leq 923K \quad (3)$$

$$\frac{L(T)}{L_0} = 9.9672 \cdot 10^{-1} + 1.179 \cdot 10^{-5} \cdot T - 2.429 \cdot 10^{-9} \cdot T^2 + 1.219 \cdot 10^{-12} \cdot T^3, T > 923K \quad (4)$$

where L_0 is the initial length at T=273 K.

The thermal axial expansion of the steel subassembly elements results in an identical fuel lower boundary for both fissile and breeder subassemblies for any expanded configuration, while the upper boundary is defined in accord to the actual fissile and fertile fuel temperatures and, in particular, differ for the HFP configuration.

The expansion of the homogenized compositions (HOM) in the model is calculated assuming the 304L diagrid steel expansion coefficient for expansion in plane and the 316Ti steel expansion coefficient for the axial expansion with corresponding correction of the density assuming material mass conservation.

The expansion of the boron carbide pellet stack is also modelled as axial expansion only with corresponding linear expansion coefficient ensuring mass conservation. There is no temperature dependence on temperature considered for the linear expansion coefficient of the boron carbide:

$$\alpha_l(T) = 5.0 \cdot 10^{-6}, [1/K]. \quad (5)$$

The corresponding axial dimension of the absorber rod body is defined by length of boron carbide absorber. The absorber pins cladding is expanded individually with the 316Ti steel expansion coefficient, while the defect of mass due to different length of the boron carbide absorber and the steel cladding is neglected. The parking position for the CSD rods is always considered as the top of fissile fuel pellet stack, while the one of the DSD rods is the top of upper fertile fuel.

4. EXPECTED CALCULATED CORE CHARACTERISTICS AND REFERENCE SOLUTION RESULTS

4.1. Serpent|JEFF311 reference benchmark solution

The described model has been implemented as an input deck for the Serpent 2 code. It is a 3D continuous-energy MC particle transport code for reactor physics application, continuously being developed by the VTT Technical Research Centre of Finland since 2004 [3]. The JEFF-3.1.1 library is used [4] which is included in the code package. The temperature-dependent model has been created applying the expansion laws as described above in Section 3.6. Input preparation was facilitated by means of the TSP tool [5]. This model has been distributed among the participants in the form of main considered configurations.

Reference calculations with the Serpent 2 code have been performed on a CSCS Cray XC40 supercomputer with $7 \cdot 10^6$ source neutrons in one cycle and $4 \cdot 10^3$ active cycles, resulting in a standard deviation of the multiplication factor of less than 1 pcm.

4.2. Criticality calculations

A set of core configurations has been considered in criticality calculations (Table 14). The four main thermal configurations described above (cases ID_{Crit}=1, 3, 10, 13) are considered: “20°C”, “180°C”, “HZP”, “HFP”. First three of them have been used for comparison with the available

experimental measurement data [2]. These cases differ by geometry due to different thermal conditions and power and provide basis for a number of additional benchmark core configurations (Table 14) which assume different nuclide temperatures and CRs position (the cases utilizing an identical thermal conditions are shaded as one group).

The calculated core configurations allow to obtain the Doppler constant calculated for different nuclide library temperatures (Table 15) and isothermal expansion coefficient and its expansion component *k* as in accord with Table 16. Reference solution results are summarized in Table 17 (the analysis of these results together with the ones obtained by the other codes is included in Section 5).

4.3. Control rods worth curve

Control rod worth curve is evaluated assuming step-wise insertion of CSD rods from -10% to 110% position with respect to the fissile height of the core, with every step of 10%. The first base configuration "$Conf_1$" is used as basis for calculations, which is the hot core geometry with cross section library temperature of 600 K and withdrawn CRs (ID_{Crit}=7). Reference solution results are summarized in Table 18.

4.4. Reactivity effects and coefficients

The set of reactivity effects and coefficients is proposed for evaluation in order to be applied in transient analysis [2]. The definitions and assumptions used for these evaluations are given below. The second base configuration "$Conf_2$" is used as basis for all calculations (which is the critical hot core geometry with CRs inserted by 40 cm (ID_{Crit}=8)) if other not specified. Reference solution results are summarized in Table 19.

4.4.1. Fuel Doppler constant

The fuel Doppler effect is a major contributor to reactivity evolution in any transient. It is calculated using the Doppler constant, defined for the whole core or its partial zones. In current benchmark activity the calculation of zone-wise Doppler constants is considered for five zones of the core: Inner core fissile fuel, outer core fissile fuel, radial blanket fertile fuel, lower axial blanket fertile fuel, upper axial blanket fertile fuel, and for the core as a whole, as result of all fuel isotopes temperature change from 600 K to 1500 K in the considered zone.

4.4.2. Sodium density coefficient

The sodium density effect is evaluated as result of density decrease by 11.04% with respect to the reference value (corresponding to sodium heat-up by 400℃ up to 800℃) inside hexcan only. The sodium density coefficient is calculated for six configurations: inner core (IC) total height, outer core (OC) total height, radial blanket (RB) total height, IC fissile height, OC fissile height, IC and OC

fissile height, where the total height stands for the axial segment from the bottom of lower axial blanket (LAB) till top of outlet section of SA.

4.4.3. Sodium void effect

The Sodium Void Effect (SVE) is evaluated as result of removal of all sodium within the hexcan at fissile fuel axial segment of SA in two following zones: IC fissile, OC fissile. In addition to the $Conf_2$ core configuration, these two SVE configuration are evaluated at the "$Conf_1$" configuration when the CRs are withdrawn.

4.4.4. Axial fuel expansion coefficient

The fuel expansion effect is modelled as result of fuel pellet stack elongation by 1.0% and 1.0% of density decrease (corresponding to temperature increase by 884℃). The fuel column elongation is considered as not linked to the cladding being fixed within the pin at the bottom of lower axial blanket. The fuel expansion coefficient is evaluated for three core configurations: IC core fertile and fissile, OC fertile and fissile, and IC, OC, RB all fuels. In order to exclude the effect of CRs insertion as result of the core height elongation, the calculations are performed at the $Conf_1$ core configuration.

4.4.5. Cladding expansion coefficient

The cladding expansion reactivity effect is modelled as result of cladding geometry and density modification due to temperature increase by 490℃ (corresponding increase by 1.0% in radial dimension and decrease by ~3.0% in density). Both axial and radial thermal expansion of the pin cladding is modelled, along with assumption, that the perturbation is considered within the fuel pellet height only, thus no other dimension change (height and axial positions of lower and upper gas plena, total pin length, etc.) except the outer and inner pin diameter is considered. Thus, the radial expansion accounts for ejection of sodium out of the in-pin-bundle space (~3.3%) due to increase of outer pin diameter. The cladding expansion coefficient is evaluated for two configurations: IC fertile and fissile, and OC fertile and fissile. Additionally, the same configurations are evaluated considering the change of construction steel cross-sections temperature considering the Doppler effect on steel isotopes.

4.4.6. Hexcan expansion coefficient

The hexcan expansion reactivity effect in modelled as result of hexcan geometry and density modification due to temperature increase by 490℃ (corresponding increase by 1.0% in radial dimensions and decrease by ~3.0% in density). The same assumption, as for the cladding effect, is taken that the perturbation is considered only within fuel height, thus there is no other dimensions change (height and axial positions of fuel column, height of sodium plenum, etc.). The effect accounts for ejection of sodium (~0.5%) due increase of hexcan volume in the core. The hexcan

expansion coefficient is evaluated for two configurations: IC fertile and fissile, and OC fertile and fissile. Additionally the same configurations are evaluated considering the change of construction steel cross-sections temperature considering the Doppler effect on steel isotopes.

4.4.7. Diagrid expansion coefficient

The diagrid expansion reactivity effect is modelled as result of diagrid thermal expansion due to temperature increase by 489°C and corresponding increase of subassembly pitch by 1%. The effect accounts for increase of sodium amount in the core, primarily as result of increase of inter-hexcan sodium volume. For the zones with input homogenized material compositions the mass conservation is considered.

4.5. Power distribution

The spatial power distribution is considered for the comparison assuming radial (SA-wise) and axial (node-wise) distributions. In the reference Serpent solution, the total power is generated and released within the fuel zones only. The axial power profile is considered on 16 equidistant axial segments individually for the IC, OC and RB as averaged along all SAs within the given core sub-zone. The reference solution for individual SA powers and axial profiles are provided in Table 20 and Table 21. The SA numbers are defined in accord to core map of Figure 1 (see also Figure 17) from left to right, from top to bottom for all fuel (non-zero power) subassemblies.

4.6. Reaction rates

The following reaction rates distributions are to be evaluated: fission rate of ^{235}U along the fertile and fissile fuel height at the position of SA in the 8th row [2]; fission rate of ^{238}U along the radial direction at axial position of 20 cm below the top of fissile fuel; fission rate of ^{239}Pu along the radial direction at axial position of 15 cm above the top of fissile fuel. The reference solution for reaction rates is provided in Table 22 and 23.

4.7. Kinetics parameters

Considering further activity on study of transient behaviour of the core, the kinetics parameters in accord with eight groups of delayed neutrons are to be evaluated, namely: prompt neutron life time, group-wise and total effective delayed neutron fractions. Reference solution for kinetics parameters is summarized in Table 24.

5. BENCHMARK RESULTS AND COMPARISONS

5.1 Neutronics solutions

Few institutions using different neutronics solutions have participated in the benchmark exercise, namely three MC solutions: SCALE623/KENO-VI|ENDFB71 (UPM), MCNP611b|JEFF311 (CIEMAT) and WIMS/MONK|JEFF311 (UCAM); and four deterministic and hybrid solutions:

WIMS/SP3|JEFF311 (UCAM), Serpent/DYN3D|JEF311 (HZDR), Serpent/PARCS|JEFF311 (GRS) and DRAGON/DONJON|JEFF311 (PSI). Solutions details are summarised hereafter.

5.1.1 SCALE623/KENO-VI|ENDFB71

KENO-VI is the 3D MC criticality module of SCALE Code System [6], developed and maintained by Oak Ridge National Laboratory. In this work, calculations were performed using the continuous-energy AMPX-formatted data provided by SCALE, in its version 6.2.3, based on the ENDF/B-VII.1 library [7]. The 3D Superphènix core model created for KENO-VI is equivalent to the Serpent model where no geometrical simplifications were made. As implemented in SCALE6.2 [8], KENO-VI has the capability of providing problem-dependent temperature corrections to the point-wise data by means of a Doppler broadening treatment so that small temperature perturbations are feasible. Continuous energy KENO-VI simulations have included $1 \cdot 10^6$ neutrons in 400 active generations and 200 skipped cycles ensuring an eigenvalue statistical uncertainty lower than 5 pcm. For those cases where reaction rates have to be tallied, the accuracy has been improved leading to an eigenvalue statistical uncertainty lower that 1.5 pcm and a maximum reaction rate uncertainty of about 0.7%.

5.1.2 MCNP611b|JEFF311

Neutronics analyses were also performed with the Monte Carlo particle transport code MCNP v6.1.1 beta [9] which is a general-purpose, continuous-energy, generalized-geometry, time-dependent, Monte Carlo radiation-transport code designed to track many particle types over broad ranges of energies. A three-dimensional complex heterogeneous geometry model and continuous energy nuclear cross section data have been used in this work. The Monte Carlo criticality calculations have been performed at CIEMAT's supercomputing machine (Xeon 5450 quadcores, 3.0 GHz) using multiprocessing capabilities. Sufficient numbers of neutrons and cycles have been considered so that overall adequate statistical uncertainties were achieved (standard value of 3 pcm in criticality calculations). The Joint Evaluated Fission and Fusion JEFF-3.1.1 nuclear data library [4] has been used for these calculations, as specified by the collaboration group.

5.1.3. WIMS/SP3|JEFF311 and WIMS/MONK|JEFF311

The WIMS/SP3 calculations were performed using a development version of the WIMS11 reactor physics code [10]. The JEFF-3.1.1 nuclear data library was used [4]. Lattice calculations are performed in 1968 energy groups for fuel assemblies, control assemblies and structural materials to generate assembly homogenized cross sections. A supercell 2D transport calculation is then performed for the control rod and surrounding fuel in 172 energy groups, to correct the cross sections for the rodded region with the superhomogenization (SPH) method. The MERLIN module within WIMS is used to perform whole core calculations using the SP3 method. A 2D RZ calculation

for the whole reactor is first performed to generate a condensing spectrum. The whole core calculation is then performed in hexagonal-Z geometry in 33 energy groups. A full description of the WIMS calculations can be found in [11].

A 3D multigroup MC WIMS/MONK calculation was also performed in hexagonal-Z geometry in 172 energy groups using the homogenized cross sections. This is useful in providing a breakdown of the discrepancies between deterministic and MC calculations due to different assumptions in the shielding, homogenization and main transport calculation.

5.1.4. Serpent/DYN3D|JEF311

The three-dimensional reactor dynamics code DYN3D [12] contains a diffusion solver for hexagonal-z geometry. This solver is based on the nodal expansion methods and multi-group approximation. Together with the Monte Carlo code Serpent [3] as a cross section generator, DYN3D proved to be a competent code for static neutronic analyses of SFR cores [13,14]. In this benchmark, the full core solutions were calculated with DYN3D while the homogenized multi-group cross sections were obtained with the Serpent code and JEFF-3.1.1 nuclear data [4].

The homogenized cross sections were generated on a 24-group energy grid [15]. Three types of the lattice level models were used to obtain the cross sections in the following core regions: (1) Non-fissile regions including blankets: 2D super-cell models [14]; (2) Fissile fuel distant in radial direction from absorbers: a 3D model containing a cluster of fully resolved fissile SA from both the inner and outer enrichment zones [14]; (3) Fissile fuel in the radial proximity of absorbers: a 3D super-cell model containing a cluster of fissile SA from both zones and a CSD in fully inserted state. The width of the models was limited to two times the SA pitch. Additionally, the cross sections of CSD, diluent and empty hexcan structure were corrected with the SPH method [16-18].

5.1.5. Serpent/ PARCS|JEFF311

The MC code Serpent 2 [3] with the JEFF-3.3.1 continuous energy library was used to build a model of the SPX core. From this model, cross-sections in 12 energy groups were generated and transformed into the NEMTAB format. In order to ensure a standard deviation smaller than 2 pcm for multiplication factors, $4 \cdot 10^3$ cycles of $2 \cdot 10^5$ neutron histories each have been simulated, the first 100 batches were discarded. The SPH method was used to generate consistent cross-sections for the diluent SAs as well as for the CSD SAs. Those cross-sections were then used with the deterministic code PARCS v 3.3.1 [19] to perform the static neutronics analysis of SPX. The geometry of the core was explicitly changed in PARCS input to take into consideration thermal expansion effects. The results have been published in [20].

5.1.6. DRAGON/DONJON|JEFF311

The DRAGON/DONJON calculations were performed using a deterministic reactor physics code package DRAGON version 5, developed at École Polytechnique de Montréal [21,22], along with the JEFF-3.1.1 nuclear data. Lattice calculations with 172 groups library were conducted with DRAGON (lattice code) using transport method to generate the homogenized 24-group energy grid [23] cross sections of different subassemblies. The full core calculations of SPX were conducted with DONJON (full core simulation code) and the homogenized 24-group cross sections, using a 3D hexagonal-z geometry. Two options were tested and applied: the SP3 option (to improve the prediction for criticality cases) and the mesh-centred finite element discretization method (MCFD) (for main scope of calculations).

The SPX subassemblies were modelled with explicit 2D geometry (pin bundles and a zone of homogenized hexcan and half inter-assembly gap) to generate its homogenized cross sections. A single subassembly model was used for fuel subassemblies (except the outermost ring of fuel region), while a super-cell model, composed of the explicitly defined target subassembly in the centre and six surrounded homogenized fuel subassemblies, were used for radial/axial breeder and control rods. Furthermore, as for the outermost ring of fuel assembly and the CSDs with a nearby diluent subassembly, some surrounded subassemblies of the super-cell model were replaced by several homogenized radial breeder subassembly or one diluent subassembly according to the actual nearby circumstances, for taking into account the neutron streaming between the target subassembly and its nearby places in the real core.

5.2. Calculation results and comparisons

In this section the main scope of results obtained by participants are presented and discussed. All the calculation results are available at Web link.

5.2.1. Criticality calculations

The resulting values of multiplication factor as in accord with Table 14 obtained with all benchmark solutions and differences from the Serpent reference one are presented in Table 25 and in Figure 6. The criticality levels of different configurations are depicted in Figure 6 with respect to the $Conf_1$. This configuration serves as a reasonable basis for evaluation of the criticality change due to a change of geometry and XS library temperature and was predicted reasonably well by all codes, except a large bias for DONJON, see Table 25) while also there is no uncertainty related to CRs insertion. The case results are combined on the plot in groups assuming four core thermal configurations described above in Section 3.6.

All codes reasonably predict isothermal expansion which main component is geometrical. Some conclusions can be drawn regarding the latter. The cases ID_{Crit}=1, 2, 5 employ identical neutron cross sections (300 K). It can be observed that different thermal states are represented reasonably

accurate by all codes assuming a uniform difference with respect to the Reference solution for all three geometries. While for the two WIMS solutions the difference for the “as fabricated” geometry (ID_{Crit}=1) is larger as compared to other configurations ID_{Crit}=2, 5. This issue was not resolved within the benchmark time framework and may require an additional investigation. For the DONJON SP3 solution, a uniform bias is observed for all three configurations. This bias of about 150 pcm is due to library temperature change from 300 K to 600 K only.

An appropriate agreement within about 120 pcm for all core configurations can be stated between the Serpent and MCNP solutions with JEFF-3.1.1 library, as well as KENO-VI with ENDFB71 library. The small differences between the Serpent and KENO-VI solutions, even when they are based on different nuclear data libraries, can be explained as result of compensation effects. In the frame of the ESFR-SMART project, it was proven that the ENDFB71 library included in SCALE6.2.3 was systematically overestimating the multiplication factor as compared to other MC codes using the same library. Firstly, one can expect that ENDFB71-based calculations predict a lower reactivity with respect to JEFF-3.1.1 for this type of reactors. However, the differences between both libraries are compensated by the observed overestimation. An analysis revealed that this issue was mainly due to the treatment of the unresolved resonance region during the AMPX processing [24]. Nonetheless, it is worth mentioning that reactivity coefficients calculated by KENO-VI appear to be valid according to the good agreement with other MC codes.

An outstanding agreement with the Reference within less than about 90 pcm is obtained for the deterministic DYN3D solution for all calculated core configurations.

The other three solutions – two deterministic: WIMS/SP3 and PARCS and one MC: WIMS/MONK – exhibit a monolithic difference from the Reference for all “unrodded” cases (all geometries and XS libraries), while overpredict the CRs worth for all cases with CRs inserted. This is clearly observed as drastic change in difference with the Reference solution for cases ID_{Crit}=6, 8, 11 with respect to corresponding “unrodded” cases ID_{Crit}=5, 7, 10. Noticeably stronger deviation (up to 8%) from the Reference is observed for all these three solutions for the configuration with fully inserted CRs (ID_{Crit}=4). The HFP configuration is also reasonably well modelled by all solutions (ID_{Crit}=13).

For the DONJON solution, all criticality values have considerable bias of about 2200-2800 pcm with respect to the reference (see Table 25). It appeared not possible to identify the reason of this deviation within the benchmark time framework. Applying the MCFD option of DONJON core solver resulted in a lower bias of about 1000-1500 pcm. However, with this option it was not possible to reproduce accurately the criticality change between cold and hot configurations. This resulted in a wrong prediction of the geometry component of the isothermal expansion

coefficient *k*. Nonetheless, both solver options provide appropriate similar results on reactivity effects and the MCFD option was used further for rest of benchmark calculations.

In Figure 7 the Doppler constant obtained for different library temperature and core configurations using data of multiplication factor calculations as in accord with definitions in Table 15 are plotted. All codes, except PARCS, are in a reasonable agreement within about 50 pcm with the Reference (less than 5%), as result of accurate prediction of corresponding criticality values. A noticeable difference for case $ID_{Doppler}$=3 is observed for the PARCS solution. DONJON underestimates the Doppler effect by about 10% for the case $ID_{Doppler}$=1. But it was found that there is no option to account for Doppler effect on non-fuel isotopes in the XS preparation procedure. With this, there is an appropriate agreement observed for the case $ID_{Doppler}$=3, where the fuel isotopes Doppler effect only is accounted for. All codes accurately predict slight deterioration of the Doppler constant for the core configuration with inserted CRs ($ID_{Doppler}$=4).

An appropriate agreement is observed between all codes of calculated isothermal expansion coefficient and its components, as shown in Figure 8. The differences from the Reference are mainly within 10% and exhibit an agreement with the data evaluated from the experiments [2].

5.2.2. Control rods worth curve

Figure 9 shows the worth curve of control rods as result of reactivity change due to simultaneous insertion of all CRs (only the CSD group is studied in the benchmark). The results demonstrate the same trends as observed for the rodded cases in criticality calculations. The MC solutions MCNP and KENO-VI and deterministic solution DYN3D demonstrate an appropriate agreement with the Reference with maximum difference up to 100 pcm for DYN3D. For both WIMS solutions and for the PARCS solution the discrepancy increases with CRs insertion. For the DONJON solution, the maximal bias is about 200 pcm for the configuration with fully inserted. One should note, that the MCFD option allowed a better agreement on CRs worth as compared to the SP3 option.

5.2.3. Reactivity effects and coefficients

5.2.3.1. Fuel Doppler constant

The Figure 10 presents a distribution of the fuel Doppler constant in different core regions. All codes demonstrate an appropriate agreement with the Reference solution within 65 pcm. For two global contributions of IC and OC the maximal difference is observed for the WIMS solutions (8% and 14% respectively) while most of other values lay within 4% deviation from the Reference.

5.2.3.2. Sodium density coefficient

Figure 11 presents results of the sodium density coefficient calculations. The results are mainly in an appropriate agreement for all codes. PARCS and DONJON solutions slightly

overestimate the effect in all cases where a large positive contribution of inner core is considered. For the inner core effect, they provide the value by up to 0.05 pcm/K (about 25% larger), while PARCS accurately predicts the effect for the outer core regions with high leakage component. This issue require further investigations. Some inconsistency was observed in the DRAGON results for the cases with fissile height voided. DRAGON predicts a lower void effect, while a decrease of the neutron leakage for these cases should result in a stronger effect, as other codes predict. The MCNP solution predicted noticeable different result for the OC (difference is equal to -0.03 pcm/K). This may be attributed to a large statistical uncertainty of result of two simulations with a small difference in reactivity. The calculated coefficient for the OC is 0.011 pcm/K and -0.020 pcm/K in Serpent and MCNP simulations respectively. The evaluated standard deviation of the sodium density effect value in Serpent calculations is about 0.004 pcm/K, while the MCNP uncertainty is higher (about 0.01 pcm/K). In addition, this situation is different for the case 5 with variation of density within the fissile height only, where an agreement can be stated for all solutions including MCNP.

5.2.3.3. Sodium void effect

Figure 12 presents the results of sodium void effect calculations. An agreement within few tens pcm is observed for two MC solutions – KENO and MCNP, as well as for deterministic solution DYN3D, except case 4 with slightly larger difference up to 70 pcm. Both WIMS solutions systematically deviate from Reference predicting a stronger positive void effect. A similar trend to overpredict the positive contribution of the Inner core is observed for PARCS solution. In the DONJON solution, the void effect for the in-pin bundle region was derived from the effect calculated for the fully voided SA assuming linearization of the effect on sodium mass, thus using a ratio of removed sodium mass inside the hexcan to the sum of inner sodium and inter wrapper sodium (which fraction is close to 20%). The DONJON solution also tends to overpredict the void effect in all configurations.

5.2.3.4. Axial fuel expansion coefficient

Figure 13 presents the results of modelling of fuel axial expansion effect. All MC solutions are in an appropriate agreement except the case 3 value calculated by MCNP. The latter result seems to have an unexpected deviation. The effect exhibits generally an additive nature and the sum of the individual contributions of the inner and outer core is equal to the whole core effect. So this deviation may be attributed to the inconsistencies in modelling or noticeably higher standard deviation for this case. The DYN3D solution is also in a very good agreement with MC ones. The results of other solutions considerably deviate from the Reference, while also do not demonstrate additivity of individual components. This may indicate the inconsistencies in the modelling approach which were not resolved within the benchmark time framework.

5.2.3.5. Cladding expansion coefficient

Figure 14 shows the results of modelling of cladding expansion effect. The effect naturally is rather small, while the consideration of the neutron cross section temperature dependency in the structure (i.e. the Doppler effect on steel isotopes) incorporates even higher uncertainty in the result. For the cases 1 and 2 with no Doppler effect accounted for all codes, except DRAGON, demonstrate an appropriate agreement with each other. The deviation for the cases 3 and 4 where the Doppler effect is accounted for is slightly stronger. The DRAGON solution provides a stronger effect for the cases with no Doppler accounted for, while the Doppler effect could not be taken into account for cases 3 and 4 as not supported in XS preparation procedure.

Accounting for Doppler effect introduce a shift by about 0.05 pcm/K for the given structure temperature variation. It results to a halving of the already naturally small effect for this core.

5.2.3.6. Hexcan expansion coefficient

In Figure 15 the results of modelling of hexcan expansion effect are shown for the similar configurations, as for the clad effect. The amount of hexcan material in the core is smaller than the clad one and the component of an ejection of sodium due hexcan expansion is less pronounced, what results in a noticeably smaller effect. The same trend is observed for the Doppler cases 3 and 4. The deterministic codes tend to overpredict the Doppler effect on steel as compared to MC codes. This effect could be practically excluded from the consideration in the reactivity balance for this core.

5.2.3.7. Diagrid expansion coefficient

The results of modelling of diagrid expansion effect are shown in Figure 16. An outstanding agreement is observed between Serpent, KENO and MCNP solutions, as well as deterministic DYN3D. Overall the difference for rest WIMS, PARCS and DRAGON solutions from reference does not exceed 25%.

5.2.4. Power distribution

Figures 17, 18 and 19 present the subassembly power distribution in the core obtained with the Serpent solution and distribution of the subassembly power along the radial core cross section. For the fissile subassemblies all available solutions are in a reasonably good agreement with the Reference (within 1-1.5% for MCNP, KENO and DYN3D, up to 2.5% for PARCS and WIMS/SP3). The DRAGON results have slightly larger deviations up to 4%. For the fertile SAs the MC solutions are within 5-7%. Deterministic solutions deviate stronger (10-15%), except the WIMS solution which predicts also within 5% and the DRAGON one which strongly overestimates power of breeder SAs. The similar magnitude of differences is observed for the power axial profile in the IC, OC and RB (Figures 20, 21, 22). For all fissile fuel nodes the difference does not exceed 3-4%, while for the axial

breeder zones and all nodes of fertile SA the differences are larger. Generally, it can be stated that all codes make a reasonably accurate prediction in the power spatial distribution of this core.

5.2.5. Reaction rates

The results on fission reaction rates of ^{235}U, ^{238}U and ^{239}Pu are depicted in Figures 23-25. Outstanding agreement within 1-2% is obtained for MC codes. The deterministic WIMS/SP3 solution provides also reasonable agreement with the reference. SCALE solution provides the same level of discrepancies for radial reaction rates distributions while larger discrepancies are observed for other solutions.

5.2.6. Kinetics parameters

Neutron kinetics parameters are summarized in Table 26 and depicted in Figure 26. Appropriate agreement can be stated between all codes for total effective delayed neutron fraction, while group contributions differ up to ~30% (for DYN3D). These results are close to the data obtained for the original core configuration close to the benchmark one. As reported in [25], effective delayed neutrons fraction in the critical core configuration evaluated with the TRIPOLI code is equal to 363±3 pcm. The corresponding prompt neutron generation time is equal to 4.75E-07 s.

5.3. Discussion

The discrepancies for selected parameters between all eight solutions were evaluated as summarized in Table 27. The data is dual corresponding to the Monte Carlo and deterministic codes domains. The value of discrepancy was defined as absolute difference between maximum and minimum of all values, while the relative discrepancy is referred to the reference value obtained with Serpent 2.

Obviously main discrepancies are observed as result of 1) the use of different methodologies and calculation routes implemented in the code like Monte Carlo or deterministic (or hybrid) methods; 2) different approximations and adaptation of the specification to the given tool (essentially important for purely deterministic methods where geometry simplifications must be introduced for core description); and 3) nuclear data implementation, i.e. different library options and evaluated files processing. One can see that applying the MC methods a generally more appropriate agreement is observed between the results. For the deterministic code domain, the differences are more pronounced. Unfortunately for both domains, there are parameters having a large discrepancy with respect to the reference value, which nature has not been resolved within the benchmark time framework.

An attempt was done to assess a potential discrepancy in case of excluding a value from the consideration which exhibits a highest difference from the reference value, as an additional uncertainty may rise also from the human factor during the code application. Corresponding filtered-

out results are compiled in the second column for every domain named as “One outlier value removed”. This exercise results in a drastic decrease of some discrepancies in the MC domain. Thus one can conclude that further improvements may be expected for the evaluated parameters. For the deterministic domain, also a noticeable decrease of discrepancies can be observed for the filtered-out set of results. Nevertheless, they stay quite large, as compared to those of the MC codes domain. As an ultimate characteristic of the results, the evaluated uncertainty of below 5-10% for most of reactivity coefficients and safety parameters and of below 230 pcm for multiplication factor could be considered as a reasonably low uncertainty of the MC codes results. The investigations are needed for understanding of a relatively large discrepancy observed for SVE and fuel axial expansion coefficient within the deterministic methods domain even applying filtered-out set of data. Appropriate agreement has been observed for other parameters of interest such as subassembly power distribution (below 4% for the fissile subassemblies), fission reaction rates, neutron kinetic data.

6. CONCLUSIONS

Within the ongoing ESFR-SMART project the benchmark activity was launched for codes validation which are applied in the project. The first phase of the benchmark was devoted to static neutronics core characterization of the French SFR Superphénix. The benchmark specification was developed and the reference solution prepared using the Monte Carlo Serpent 2 code. The specification was distributed to the participants also in the form of Serpent 2 input deck in order to minimize any potential inaccuracies in use of the benchmark data. The reference solution includes the multiplication factor for selected core configurations, power distributions, reaction rates distributions, control rod worth curve, reactivity coefficients and safety parameters, neutron kinetic data.

Seven other solutions were also delivered for the core neutronic characterization including application of different Monte Carlo and deterministic methods. The comparisons were performed with the reference solution and potential reasons of differences were discussed.

The core characterization data obtained within the first phase of the benchmark will be further used in the second phase for modelling of transient behaviour of the core.

FUNDING

The work has been prepared within EU Project ESFR-SMART, which has received funding from the EURATOM Research and Training Programme 2014-2018 under the Grant Agreement No. 754501.

ACKNOWLEDGEMENTS

Reference solution calculations have been performed with use of Cray XC40 supercomputer resources supported by a grant from the Swiss National Supercomputing Centre (CSCS) under Project s771 “Generation-IV European Sodium Fast Reactor: Computation of the Core Parameters Using a High-Fidelity Monte Carlo Code”.

REFERENCES

[1] Mikityuk, K., Girardi, E., Krepel, J., Bubelis, E., Fridman, E., Rineiski, A., and Girault, N., 2017. "ESFR-SMART: new Horizon-2020 project on SFR safety", In Int. Conf. on Fast Reactors and Related Fuel Cycle: Next Generation Nuclear Systems for Sustainable Development (FR17).

[2] Ponomarev, A., Bednarova, A., and Mikityuk, K., 2018, "New sodium fast reactor neutronics benchmark", Proc. of PHYSOR 2018, Cancun, Mexico, April 22-26, 2018.

[3] Leppanen, J., Pusa, M., Viitanen, T., Valtavirta, V., and Kaltiaisenaho, T., 2015, "The Serpent Monte Carlo code: Status, development and applications in 2013", Annals of Nuclear Energy, Vol. 82, pp. 142-150.

[4] Santamarina, A., Bernard, D., Blaise, P., Coste, M., Courcelle, A., Huynh, T.D., Jouanne, C., Leconte, P., Litaize, O., Mengelle, S., Noguère, G., Ruggiéri, J-M., Sérot, O., Tommasi, J., Vaglio, C., Vidal, J-F., and Rugama, Y., 2009, "The JEFF-3.1.1 Nuclear Data Library - JEFF Report 22 - Validation Results from JEF-2.2 to JEFF-3.1.1", NEA No. 6807, 2009, https://www.oecd-nea.org/dbdata/nds_jefreports/jefreport-22/nea6807-jeff22.pdf.

[5] Travleev, A., 2013, "TSP: Python Package to Facilitate Preparation of Input Files", Internal report INR 31/13 – NUKLEAR 3462, KIT, Karlsruhe, Germany, November 2013.

[6] Rearden, B. T., and Jessee, M. A., 2016, "SCALE Code System," Ornl/Tm-2005/39, no. 6.2.3, Oak Ridge National Laboratory (ORNL), Oak Ridge, TN, United States, p. 2747, 2016, DOI: 10.2172/1408010.

[7] Chadwick, M. B., Herman, M., Obložinský, P., Dunn, M.E., Danon, Y., Kahler, A. C., Smith, D.L., Pritychenko, B., Arbanas, G., Arcilla, R., Brewer, R., Brown, D.A., Capote, R., Carlson, A.D., Cho, Y.S., Derrien, H., Guber, K., Hale, G.M., Hoblit, S., Holloway, S., Johnson, T.D., Kawano, T., Kiedrowski, B.C., Kim, H., Kunieda, S., Larson, N.M., Leal, L., Lestone, J.P., Little, R.C., McCutchan, E.A., MacFarlane, R.E., MacInnes, M., Mattoon, C.M., McKnight, R.D., Mughabghab, S.F., Nobre, G.P.A., Palmiotti, G., Palumbo, A., Pigni, M.T., Pronyaev, V.G., Sayer, R.O., Sonzogni, A.A., Summers, N.C., Talou, P., Thompson, I.J., Trkov, A., Vogt, R.L., van der Marck, S.C., Wallner, A., White, M.C., Wiarda, D., and Young, P.G., 2011, "ENDF/B-VII.1 Nuclear Data for Science and Technology: Cross Sections, Covariances, Fission Product Yields and Decay Data", Nuclear Data Sheets, Vol. 112, No. 12, pp. 2887–2996, December 2011, DOI: 10.1016/J.NDS.2011.11.002.

[8] Rearden, B. T., Petrie, L.M., Peplow, D.E., Bekar, K.B., Wiarda, D., Celik, C., Perfetti, C.M., Ibrahim, A.M., Hart, S.W.D., Dunn, M.E., and Marshall, W.J., 2015, "Monte Carlo capabilities of the SCALE code system," Annals of Nuclear Energy, Vol. 82, pp. 130–141, August 2015, DOI: 10.1016/j.anucene.2014.08.019.

[9] Pelowitz, D. B., 2014, “MCNP6 User’s Manual, Code version 6.1.1beta”, LA-CP-14-00745, Los Alamos National Laboratory, USA, 2014.
[10] Lindley, B., Hosking, G., Smith, P., Powney, D., Tollit, B., Fry, T., Perry, R., Ware, T., Murphy, C., Grove, C., Thomas, M., Hesketh, K., and Kotlyar, D., 2017, “Developments with the WIMS Reactor Physics Code for Whole Core Calculations”, Proc. of M&C2017, Jeju, Korea, April 16-20, 2017.
[11] Davies, U., Lindley, B., Tollit, B., and Shwageraus, E., 2019, “Whole-core validation of the Superphénix Reactor using WIMS11 and an investigation into a hybrid RZ-HEX SP3 calculation route”, Proc. of M&C2019, Portland, OR, August 25-29, 2019.
[12] Rohde, U., Kliem, S., Grundmann, U., Baier, S., Bilodid, Y., Duerigen, S., Fridman, E., Gommlich, A., Grahn, A., Holt, L., Kozmenkov, Y., and Mittag, S.,2016, “The reactor dynamics code DYN3D – models, validation and applications”, Progress in Nuclear Energy, Vol. 89, pp. 170–190, 2016, DOI: 10.1016/j.pnucene.2016.02.013.
[13] Nikitin, E., and E. Fridman, 2018, “Extension of the reactor dynamics code DYN3D to SFR applications – Part II: Validation against the Phenix EOL control rod withdrawal tests”, Annals of Nuclear Energy, Vol. 119, pp. 411–418, September 2018, DOI: 10.1016/j.anucene.2018.05.016.
[14] Nikitin E., and Fridman E., 2019, “Modeling of the FFTF isothermal physics tests with the Serpent and DYN3D codes”, Annals of Nuclear Energy, Vol. 132, pp. 679–685, October 2019, DOI: 10.1016/j.anucene.2019.06.058.
[15] Fridman E., and Shwageraus, E., 2013, “Modeling of SFR cores with Serpent-DYN3D codes sequence”, Annals of Nuclear Energy, Vol. 53, pp. 354–363, March 2013, DOI: 10.1016/j.anucene.2012.08.006.
[16] Hebert, A., 1993, “Consistent technique for the pin-by-pin homogenization of a pressurized water reactor assembly”, Nuclear Science and Engineering, Vol. 113, No. 3, pp. 227–238, 1993.
[17] Kavenoky, A., 1978, “The SPH Homogenization Method”, in A Specialists’ Meeting on Homogenization Methods in Reactor Physics, IAEA-TECDOC-231, 1978.
[18] Nikitin, E., Fridman, E., and Mikityuk, K., 2015, “On the use of the SPH method in nodal diffusion analyses of SFR cores”, Annals of Nuclear Energy, Vol. 85, pp. 544–551, November 2015, DOI: 10.1016/j.anucene.2015.06.007.
[19] Downar, T.J. , Barber, D.A., Miller, R.M.R., Lee, C., Kozlowski, T., Lee, D., Xu, Y., Gan, J., Joo, H.G., Cho, J.Y., Lee, K., Ulses, A.P., 2002, “PARCS: Purdue Advanced Reactor Core Simulator”, Proc. of PHYSOR-2002, Seoul, Korea, October 7-10, 2002.
[20] Henry, R., Seubert, A., 2019, “3-D modelling of a Superphénix benchmark with Serpent and PARCS for coupled simulation with PARCS/ATHLET”, Proc. of the M&C2019, Portland, OR, USA, August 25-29, 2019.

[21] Marleau, G., Hébert, A. and Roy R., 1992, “New Computational Methods Used in the Lattice Code Dragon”, Proc. Int. Topl. Mtg. on Advances in Reactor Physics, Charleston, USA, March 8–11, 1992, American Nuclear Society. (DRAGON can be downloaded from the web site at http://www.polymtl.ca/merlin/)

[22] Hébert, A., 2013, “DRAGON5: Designing Computational Schemes Dedicated to Fission Nuclear Reactors for Space”, Int. Conf. on Nuclear and Emerging Technologies for Space, Albuquerque, NM, February 25–28, 2013.

[23] Faure, B., Marleau, G., 2017, “Simulation of a sodium fast core: Effect of B1 leakage models on group constant generation”, Annals of Nuclear Energy, Vol. 99, pp. 484-494, January 2017.

[24] Jiménez-Carrascosa, A., Fridman, E., García-Herranz, N., Alvarez-Velarde, F., Romojaro, P., Bostelmann, F., 2019, “About the impact of the Unresolved Resonance Region in Monte Carlo simulations of Sodium Fast Reactors,” Proc. of ICAPP-2019, Juan-les-Pins, France, May 12-15, 2019, https://doi.org/10.5281/zenodo.3324476.

[25] Garcia-Cervantes, E.-Y., 2019, “Modeling and analysis of power fast reactors tests for the neutronic calculation scheme APOLLO-3®-SFR applied to the ASTRID reactor”, Ph.D. dissertation, FRCEA-TH-12142, France, 2019.

ACRONYMS AND ABBREVIATIONS

2D	two dimensional
3D	three dimensional
CE	Continuous Energy
CR	Control Rod
CSD	Control and Shutdown Device
DSD	Diverse Shutdown Device
IC	Inner Core
HFP	Hot Full Power
HZP	Hot Zero Power
MC	Monte Carlo
MOX	Mixed Oxide (nuclear fuel)
LAB	Lower Axial Blanket
OC	Outer Core
pcm	per cent mille or 10-5 (is equal to one-thousandth of a percent of the reactivity)
RB	Radial Blanket
SA	SubAssembly
SFR	Sodium cooled Fast Reactor
SPH	Superhomogenization
SPX	French sodium cooled fast reactor Superphénix

SVE	Sodium Void Effect
UAB	Upper Axial Blanket
UGP	Upper Gas Plenum
XS	neutron cross sections

Figure Captions List

Fig. 25 Normalized Pu-239 fission rate (hollow markers refer to the Y-axis to the left) and difference from reference (dashed lines refer to the Y-axis to the right)

Fig. 26 Group delayed neutron fraction (bars refer to the Y-axis to the left) and difference from reference (dashed lines refer to the Y-axis to the right)

Table Caption List

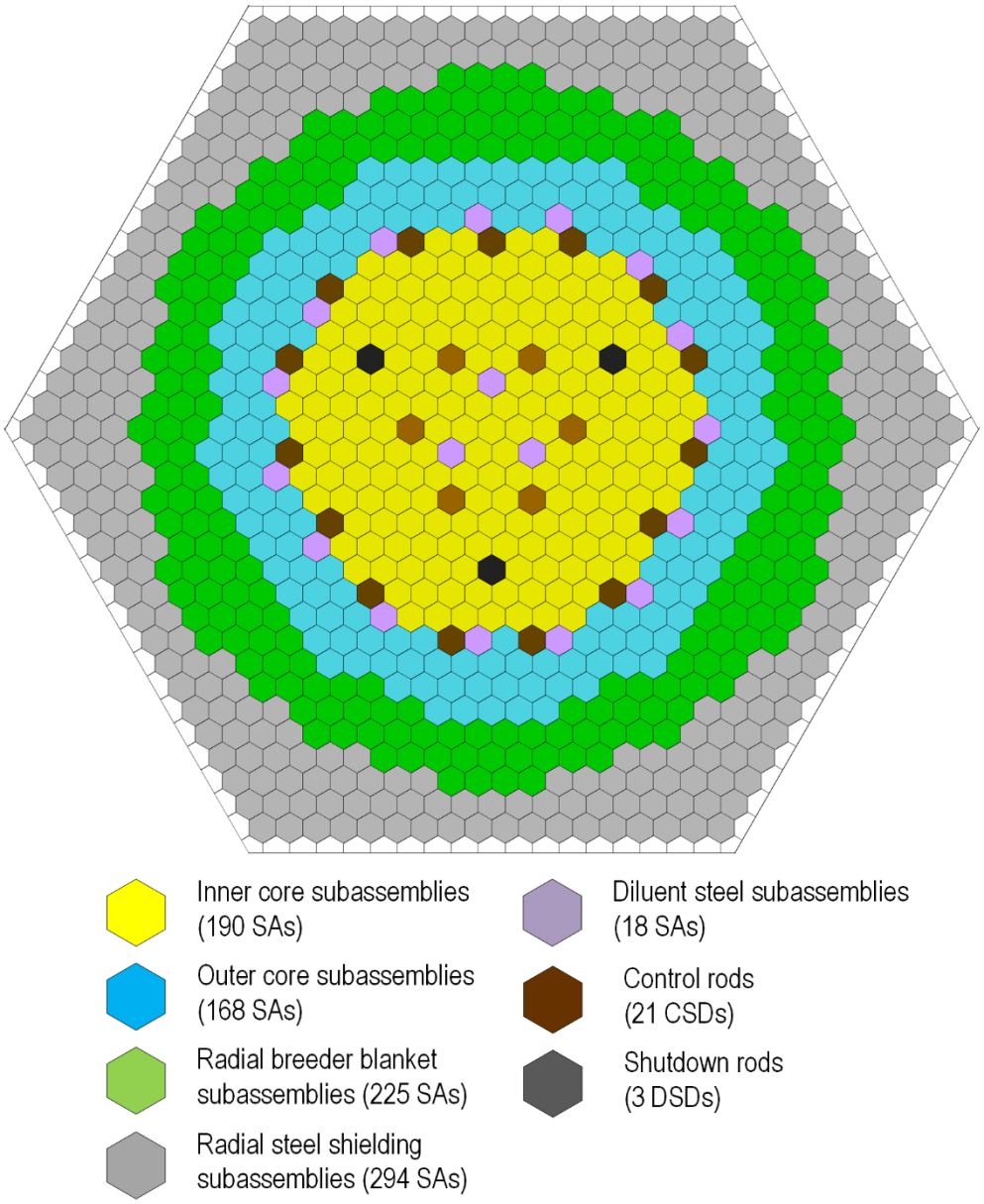

Figure 1. Radial core layout

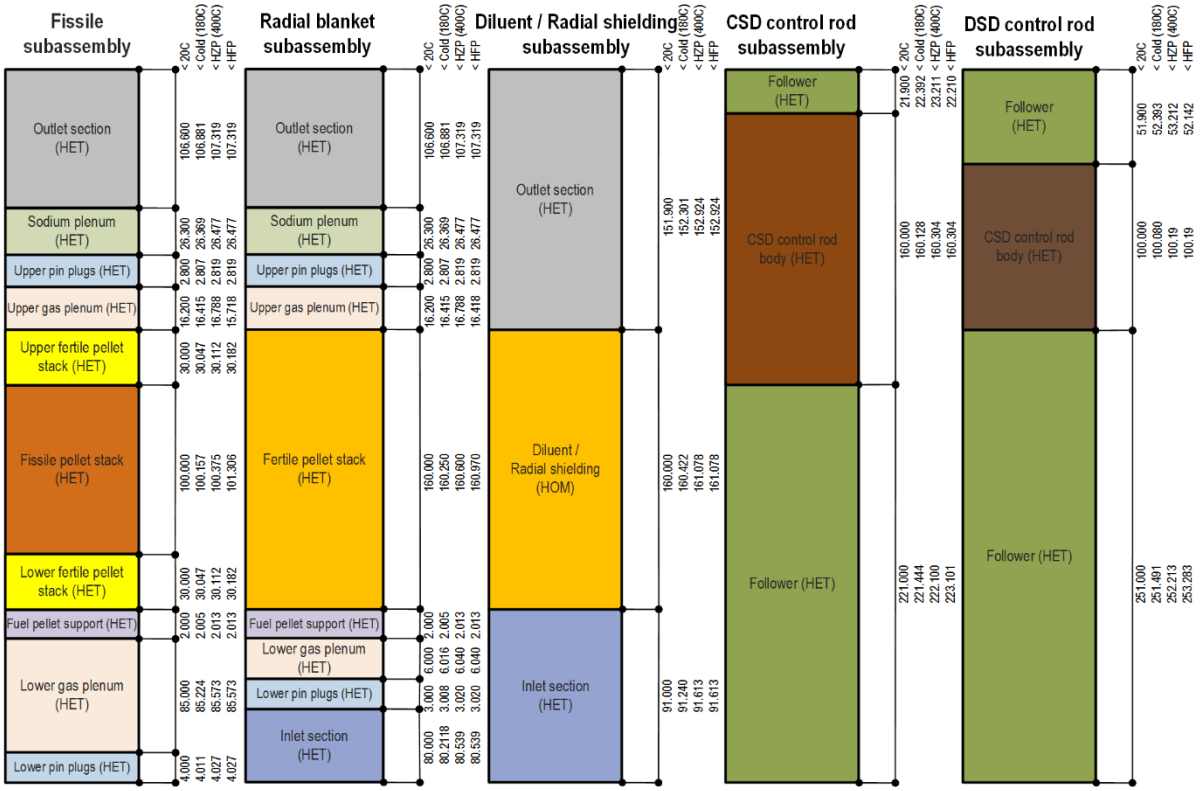

Figure 2. Axial layout of subassemblies (dimensions are given in cm)

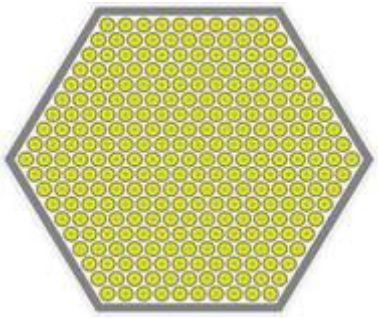

Figure 3. Fissile subassembly cross section of the pin bundle with fissile pellet

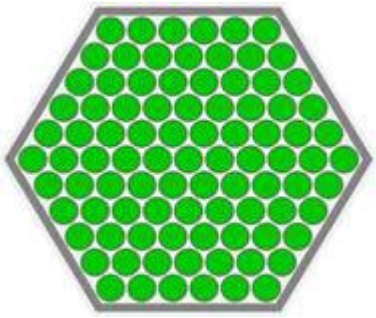

Figure 4. Radial breeder blanket subassembly cross section

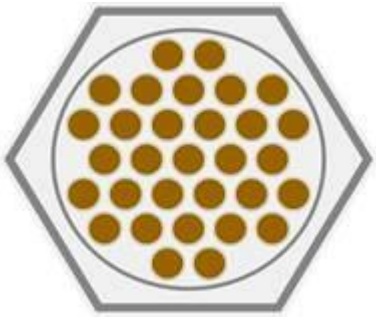

Figure 5. Control and shutdown absorber rod cross section

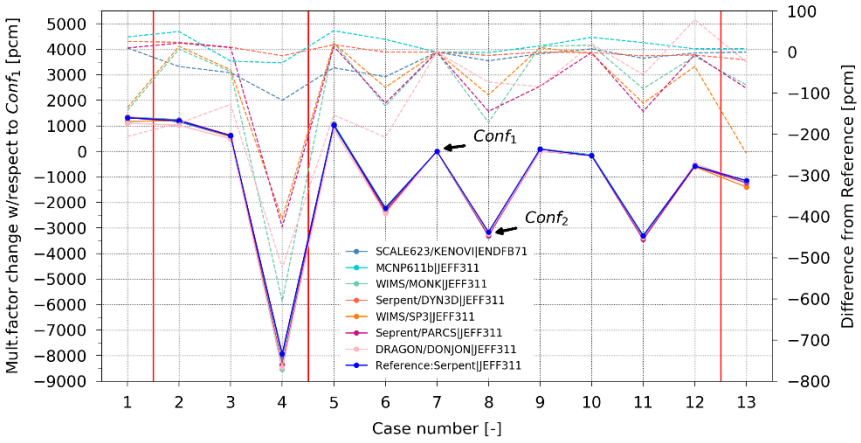

Case	CR insertion [cm]	XS temperature/Geometry [K] Fissile	Fertile	Others	Case	CR insertion [cm]	XS temperature/Geometry [K] Fissile	Fertile	Others
1	0	300/293	300/293	300/293	8	40	600/673	600/673	600/673
2	0	300/453	300/453	300/453	9	0	600/673	600/673	300/673
3	0	453/453	453/453	453/453	10	0	673/673	673/673	673/673
4	100	453/453	453/453	453/453	11	40	673/673	673/673	673/673
5	0	300/673	300/673	300/673	12	0	900/673	900/673	900/673
6	40	300/673	300/673	300/673	13	0	1500/1500	900/900	600/673
7	0	600/673	600/673	600/673					

Figure 6. Results of multiplication factor for different benchmark solutions: multiplication factor change with respect to $Conf_1$ (solid lines refer to the Y-axis to the left) and difference from reference (dashed lines refer to the Y-axis to the right)

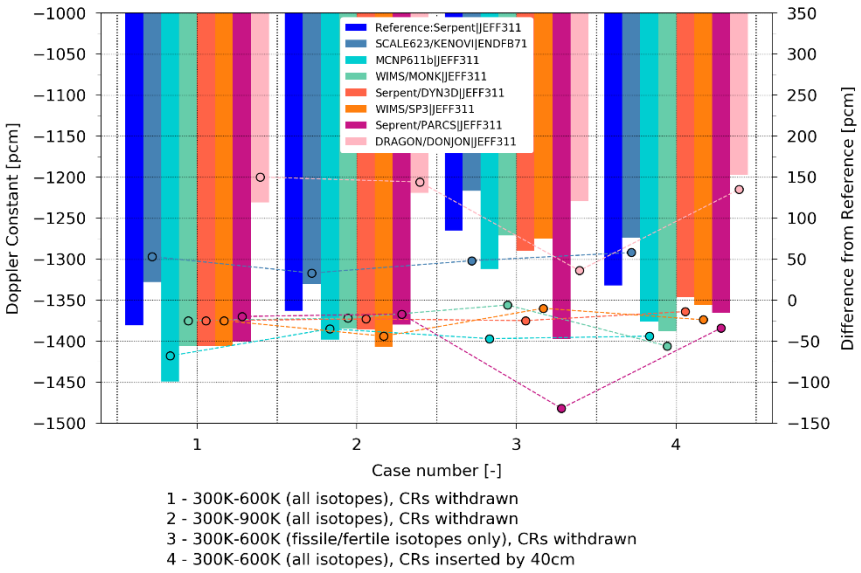

Figure 7. Doppler constant (bars refer to the Y-axis to the left) and difference from reference (dashed lines refer to the Y-axis to the right) calculated for different conditions

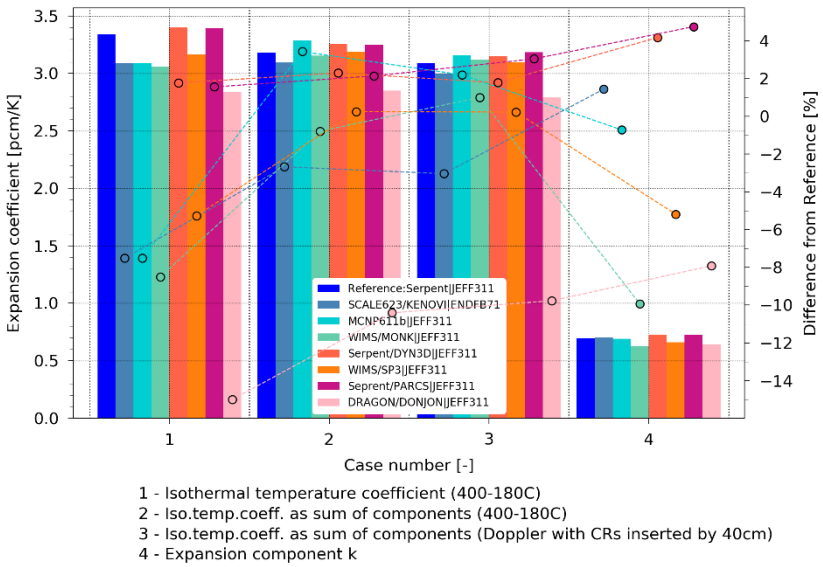

Figure 8. Isothermal expansion coefficient and its components (bars refer to the Y-axis to the left) and difference from reference (dashed lines refer to the Y-axis to the right)

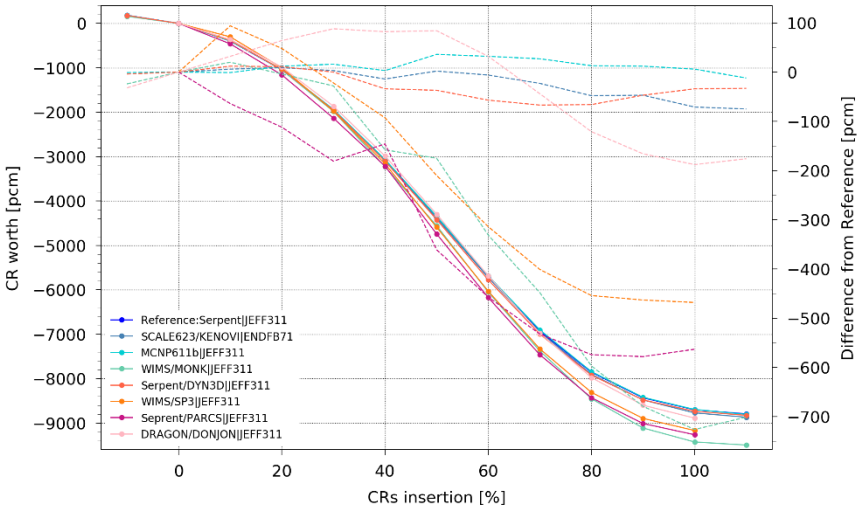

Figure 9. Control rods worth curve (solid lines refer to the Y-axis to the left) and difference from reference (dashed lines refer to the Y-axis to the right)

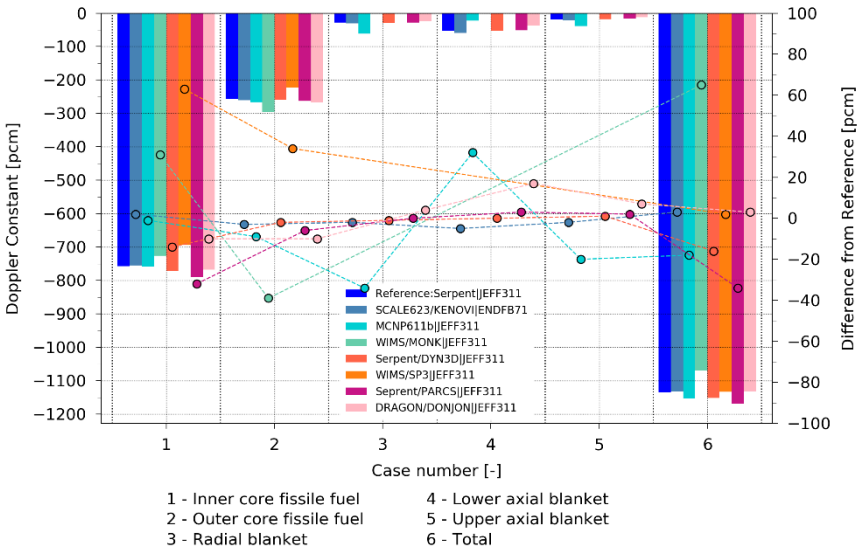

Figure 10. Fuel Doppler constant for different core zones (bars refer to the Y-axis to the left) and difference from reference (dashed lines refer to the Y-axis to the right)

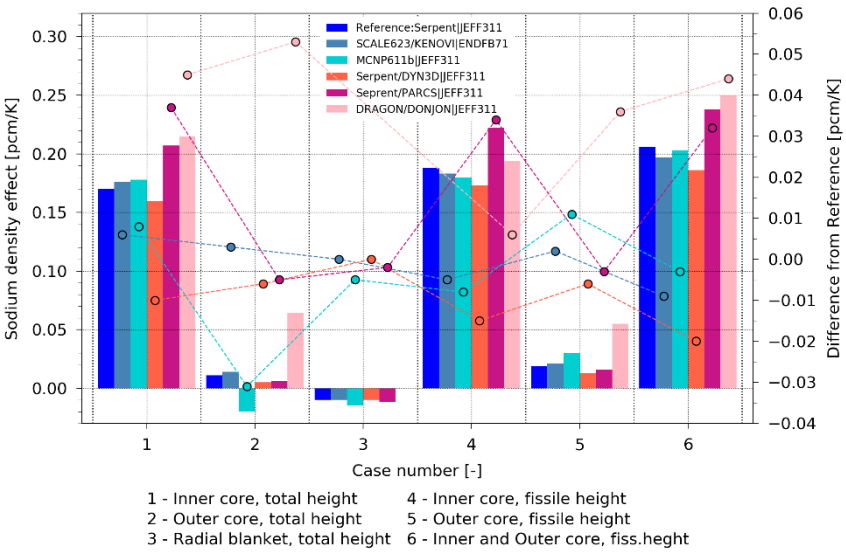

Figure 11. Sodium density coefficient for different core configurations (bars refer to the Y-axis to the left) and difference from reference (dashed lines refer to the Y-axis to the right)

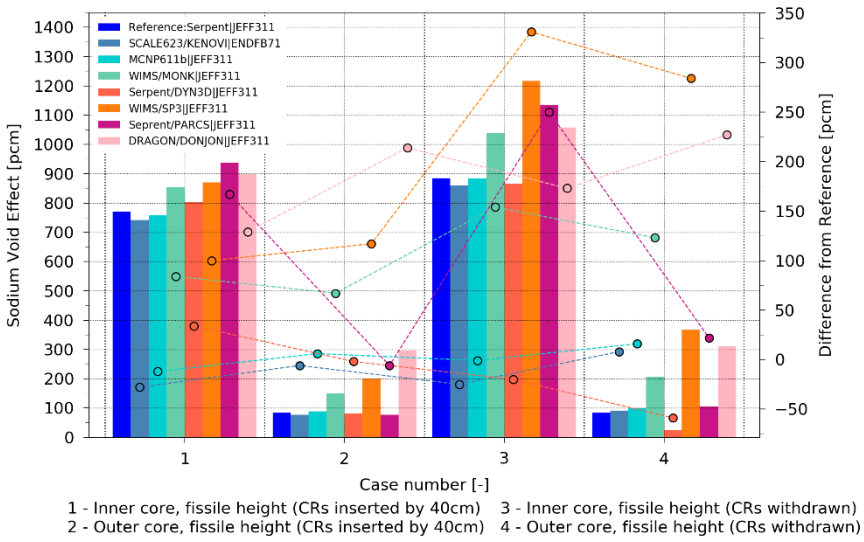

Figure 12. Sodium void effect for different core configurations (bars refer to the Y-axis to the left) and difference from reference (dashed lines refer to the Y-axis to the right)

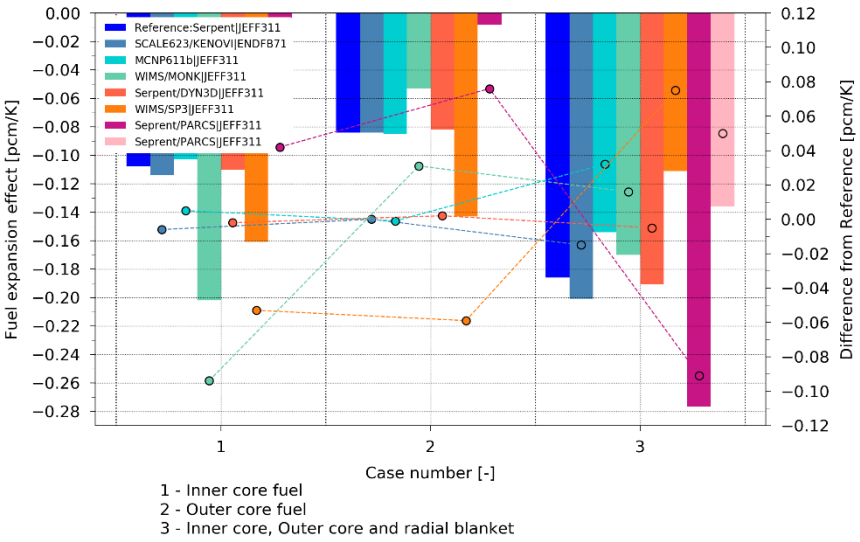

Figure 13. Axial fuel expansion coefficient (bars refer to the Y-axis to the left) and difference from reference (dashed lines refer to the Y-axis to the right)

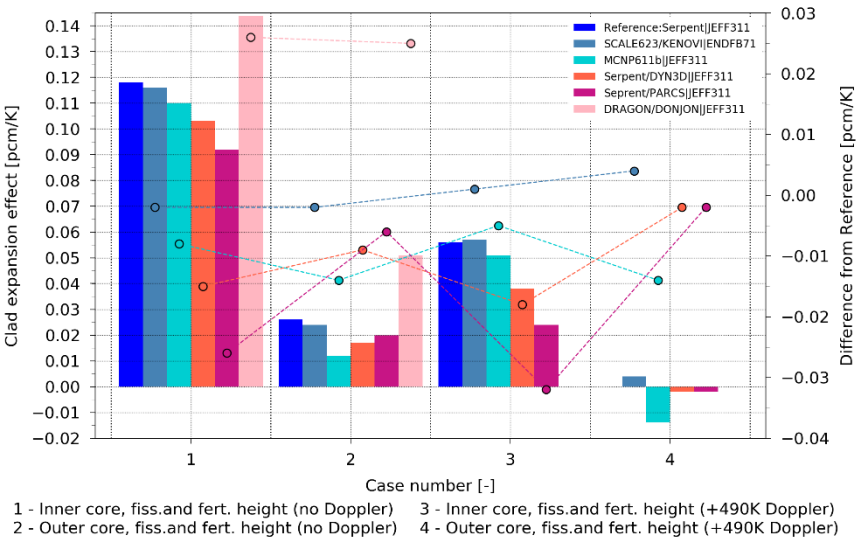

Figure 14. Clad expansion effect (bars refer to the Y-axis to the left) and difference from reference (dashed lines refer to the Y-axis to the right)

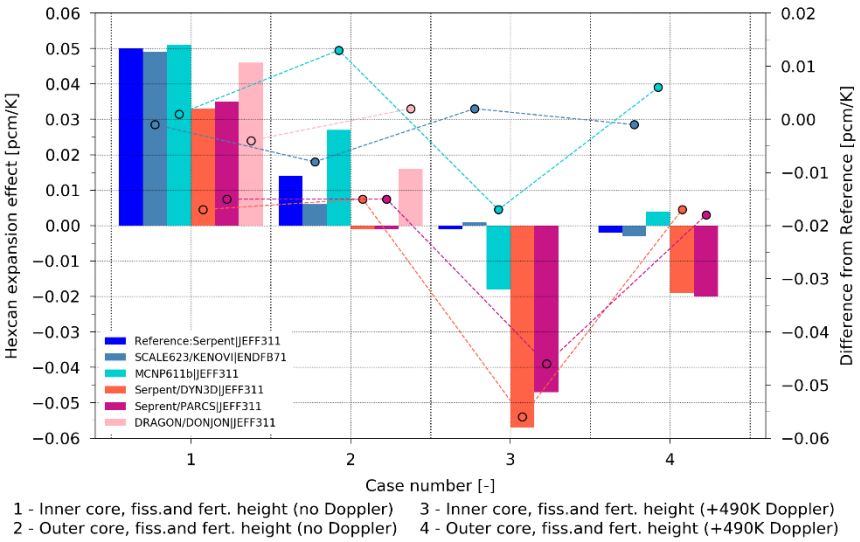

Figure 15. Hexcan expansion effect (bars refer to the Y-axis to the left) and difference from reference (dashed lines refer to the Y-axis to the right)

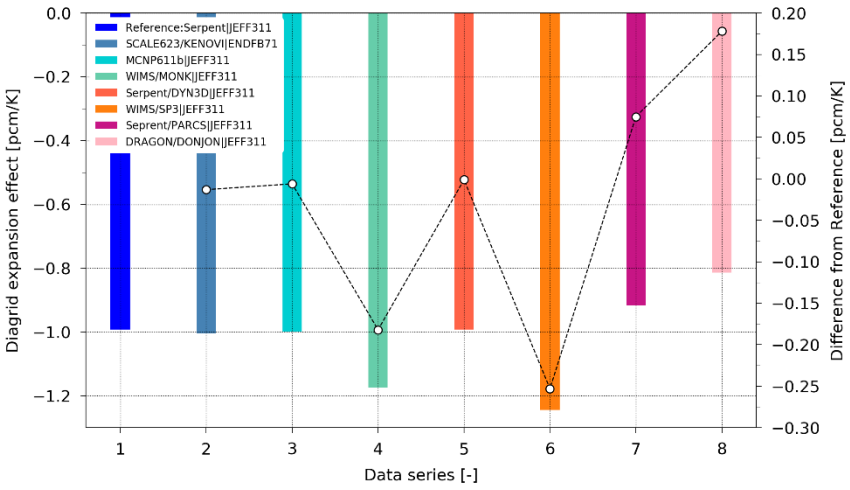

Figure 16. Diagrid expansion effect (bars refer to the Y-axis to the left) and difference from reference (dashed lines refer to the Y-axis to the right)

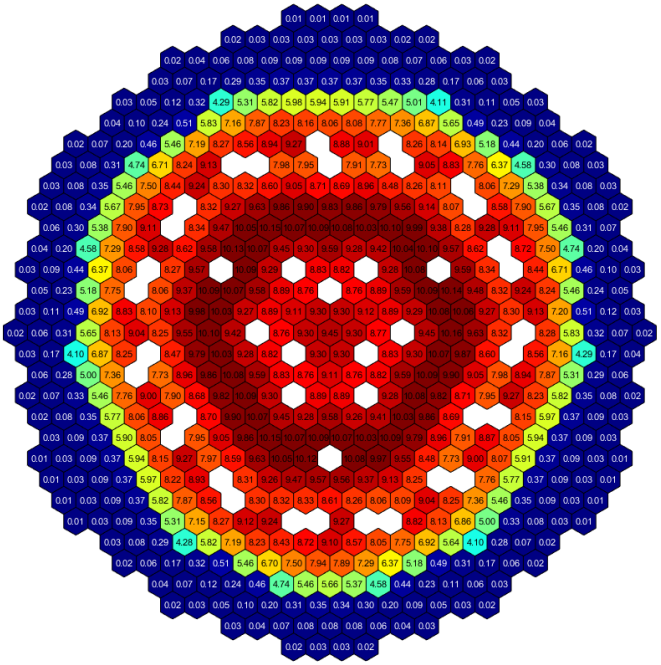

Figure 17. Subassembly power map for Reference Serpent calculation

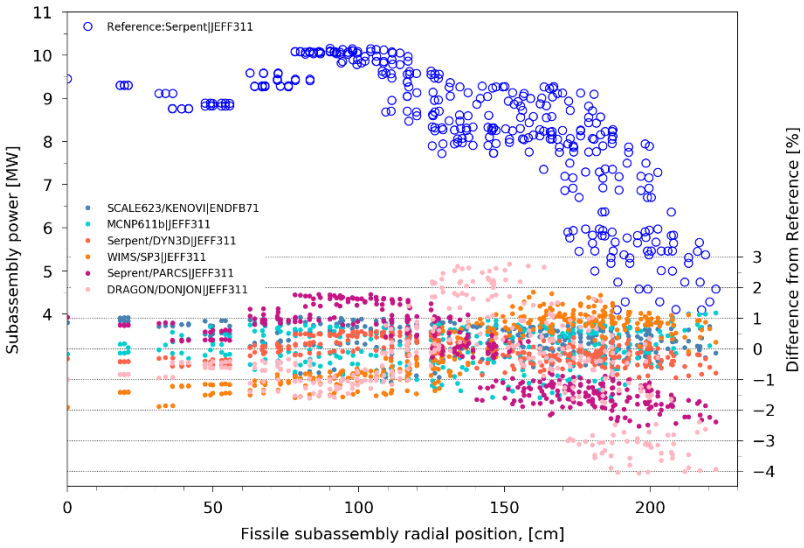

Figure 18. Fissile subassembly power values versus radial position for Serpent (hollow circles refer to the Y-axis to the left) and difference from Reference for other solutions (filled circles refer to the Y axis to the right)

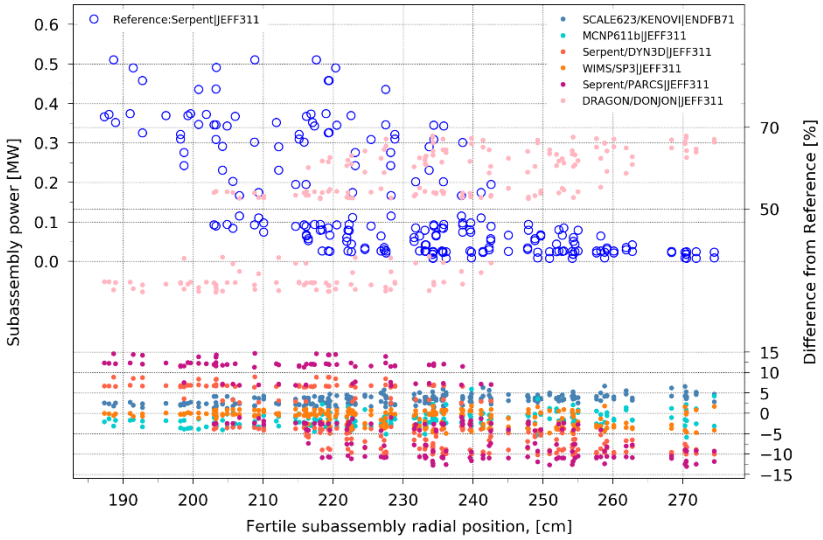

Figure 19. Radial fertile blanket subassembly power values versus radial position for Serpent (hollow circles refer to the Y-axis to the left) and difference from Reference for other solutions (filled circles refer to the Y axis to the right)

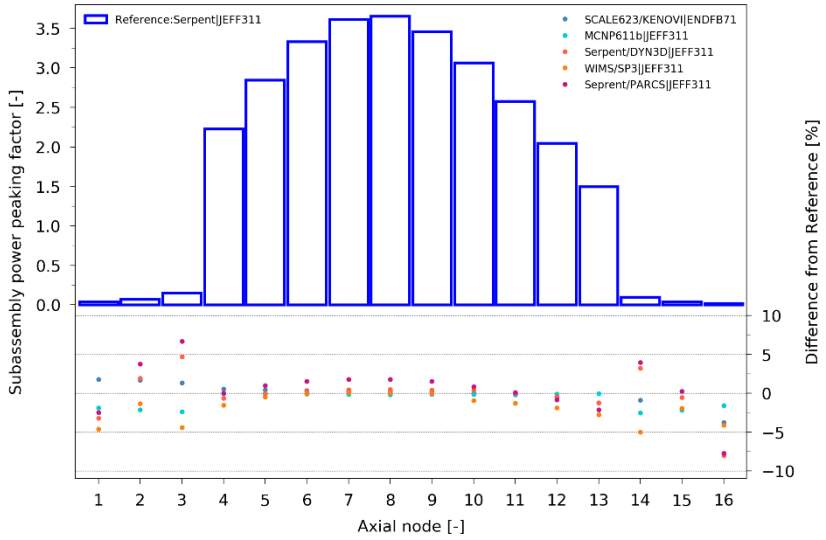

Figure 20. Averaged axial power profile in the Inner Core for Serpent (bars refer to the Y-axis to the left) and difference from Reference for other solutions (filled circles refer to the Y axis to the right)

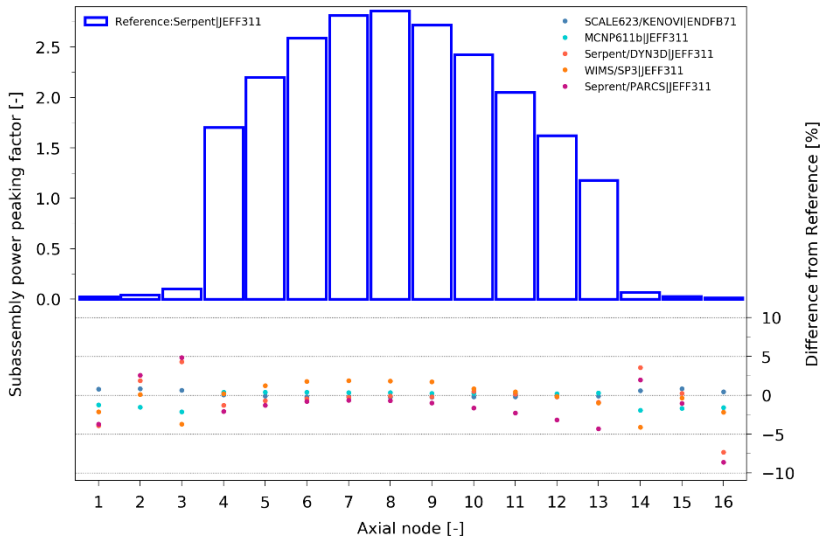

Figure 21. Averaged axial power profile in Outer core for Serpent (bars refer to the Y-axis to the left) and difference from Reference for other solutions (filled circles refer to the Y axis to the right)

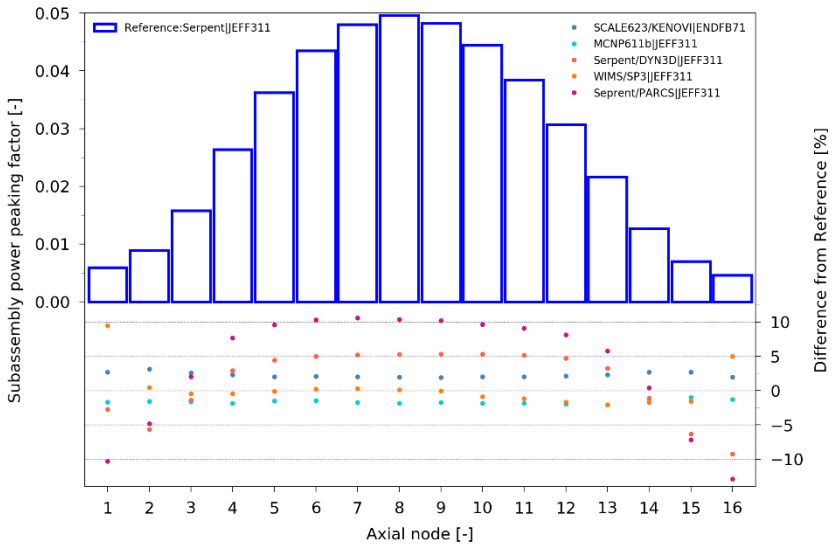

Figure 22. Averaged axial power profile in Radial Breeder Blanket for Serpent (bars refer to the Y-axis to the left) and difference from Reference for other solutions (filled circles refer to the Y axis to the right)

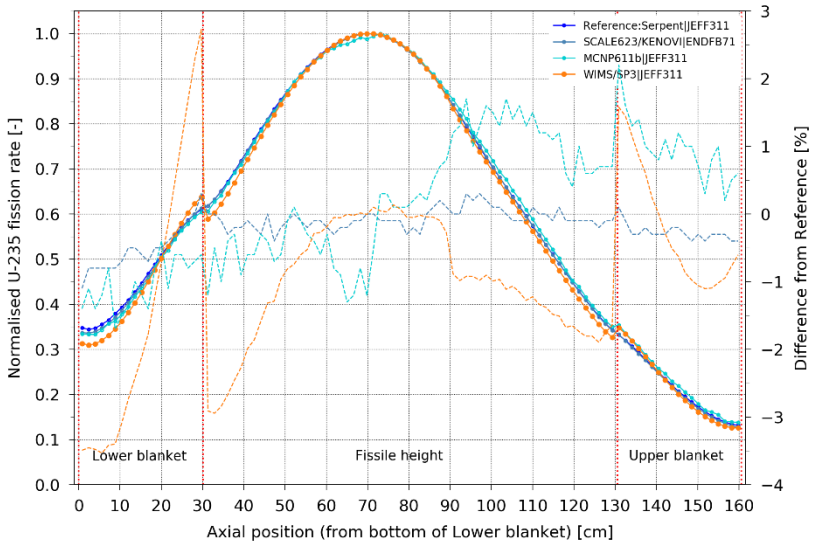

Figure 23. Normalized U-235 fission rate (solid lines refer to the Y-axis to the left) and difference from reference (dashed lines refer to the Y-axis to the right)

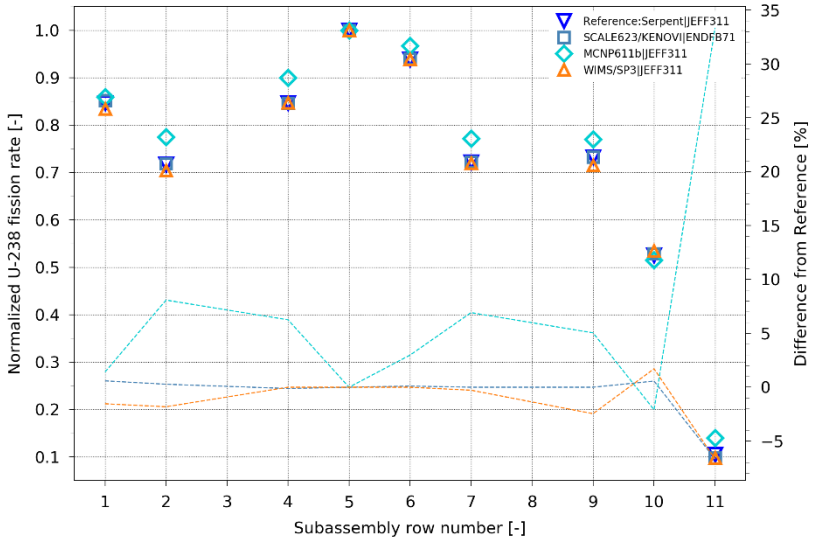

Figure 24. Normalized U-238 fission rate (hollow markers refer to the Y-axis to the left) and difference from reference (dashed lines refer to the Y-axis to the right)

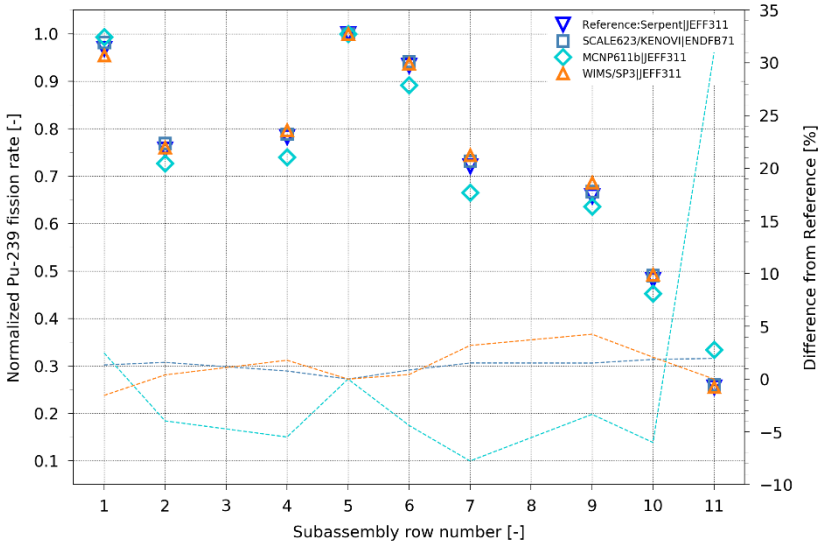

Figure 25. Normalized Pu-239 fission rate (hollow markers refer to the Y-axis to the left) and difference from reference (dashed lines refer to the Y-axis to the right)

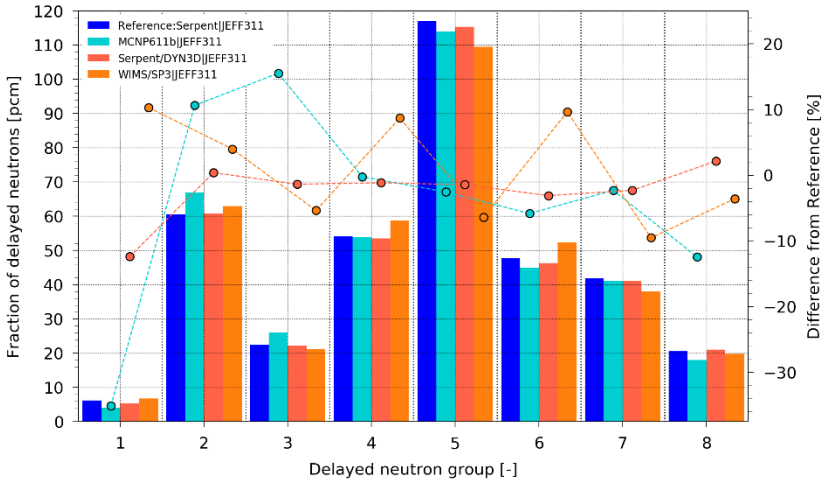

Figure 26. Group delayed neutron fraction (bars refer to the Y-axis to the left) and difference from reference (dashed lines refer to the Y-axis to the right)

Table 1. General characteristics of Superphénix reactor

Parameter	Value
Thermal / electric power, MW	3000 / 1240
Average fissile / fertile fuel temperature, °C	1227 / 627
Primary sodium inlet / outlet temperature, °C	395 / 545
Fissile/fertile fuel type	$(U,Pu)O_2$ / UO_2
Fissile fuel enrichment in the inner / outer fuel regions, %	16.0*/19.7*
Total mass of plutonium in the fissile core, kg	5780
Mass of ^{239}Pu isotope in the fissile core, kg	4054
Mass of ^{235}U isotope in the fissile core, kg	142
Volume of the fissile core, m^3	10.75
Equivalent diameter of the fissile core, m	3.70
Height of the fissile pellet stack, m	1.00
Height of the lower/upper breeder blanket, m	0.30 / 0.30
Height of the radial blanket fertile pellet stack, m	1.60
Number of subassemblies in the inner/outer fuel regions	193**/171**
Number of subassemblies in the radial breeder blanket	234**
Number of control / shutdown rods (CSD/DSD)	21 / 3
Subassembly pitch in the diagrid, mm	179.0

(*) Enrichment is defined as a ration of mass of ^{235}U and all Pu isotopes to mass of all heavy metal isotopes, differs from the one considered in the benchmark for start-up core

(**) Values differ from considered start-up core configuration, see Figure 1

Table 2. Fissile subassembly parameters

Parameter	“20°C”	“180°C”	“HZP”	“HFP”
Subassembly pitch, cm	17.9	17.946	18.018	18.018
Hexcan outer flat-to-flat size, cm	17.3	17.346	17.417	17.417
Hexcan wall thickness, cm	0.45	0.4512	0.4530	0.4530
Pin pitch, cm	0.98	0.9826	0.9866	0.9866
Pin cladding inner diameter, cm	0.737	0.7389	0.7420	0.7420
Pin cladding outer diameter, cm	0.8584	0.8607	0.8642	0.8642
Fissile fuel pellet diameter, cm	0.714	0.714*	0.714*	0.714*
Fissile fuel pellet inner hole diameter, cm	0.2	0.2*	0.2*	0.2*
Fertile pellet diameter, cm	0.707	0.707*	0.707*	0.707*
Outlet sleeve inner diameter, cm	7.0	7.0185	7.0472	7.0472

(*) The fuel pellet radial dimensions are kept “as fabricated” while the density is corrected in accord with axial expansion as corresponding to considered thermal core state in order to ensure the fuel mass conservation

Table 3. Fertile subassembly parameters

Parameter	“20°C”	“180°C”	“HZP”	“HFP”
Subassembly pitch, cm	17.9	17.946	18.018	18.018
Hexcan outer flat-to-flat size, cm	17.3	17.346	17.417	17.417
Hexcan wall thickness, cm	0.45	0.4512	0.4530	0.4530
Pin pitch, cm	1.69	1.6945	1.7014	1.7014
Pin cladding inner diameter, cm	1.466	1.4699	1.4759	1.4759
Pin cladding outer diameter, cm	1.5835	1.5877	1.5942	1.5942
Fertile pellet diameter, cm	1.436	1.436*	1.436*	1.436*
Outlet sleeve inner diameter, cm	7.0	7.0185	7.0472	7.0472

(*) The fuel pellet radial dimensions are kept “as fabricated” while the density is corrected in accord with axial expansion as corresponding to considered thermal core state in order to ensure the fuel mass conservation

Table 4. CSD and DSD subassembly parameters

Parameter	“20°C”	“180°C”	“HZP”	“HFP”
Subassembly pitch, cm	17.9	17.946	18.018	18.018
Hexcan outer flat-to-flat size, cm	17.3	17.346	17.417	17.417
Hexcan wall thickness, cm	0.45	0.4512	0.4530	0.4530
Pin pitch, cm	2.277	2.2788	2.2813	2.2813
Pin cladding inner diameter, cm	1.8	1.8048	1.8121	1.8121
Pin cladding outer diameter, cm	1.9	1.9050	1.9128	1.9128
Absorber pellet diameter, cm	1.7	1.7*	1.7*	1.7*
Rod body outer diameter, cm	14.9	14.9393	15.0004	15.0004
Rod body inner diameter, cm	14.5	14.5383	14.5977	14.5977

(*) The boron carbide pellet radial dimensions are kept “as fabricated” while the density is corrected in accord with axial expansion as corresponding to considered thermal core state in order to ensure the boron carbide mass conservation

Table 5. Isotope number densities of the inner core fissile fuel

Isotope	Number density, $\times 10^{24}$ cm^{-3}			
	"20°C"	"180°C"	"HZP"	"HFP"
U-235	1.01274E-04	1.01116E-04	1.00896E-04	9.99687E-05
U-238	1.98991E-02	1.98680E-02	1.98248E-02	1.96426E-02
Pu-238	1.78335E-05	1.78056E-05	1.77669E-05	1.76036E-05
Pu-239	2.45976E-03	2.45592E-03	2.45058E-03	2.42806E-03
Pu-240	7.33391E-04	7.32245E-04	7.30653E-04	7.23938E-04
Pu-241	1.97174E-04	1.96866E-04	1.96438E-04	1.94633E-04
Pu-242	6.84331E-05	6.83261E-05	6.81776E-05	6.75511E-05
Am-241	4.82584E-05	4.81830E-05	4.80782E-05	4.76364E-05
O	4.65798E-02	4.65070E-02	4.64059E-02	4.59794E-02

Table 6. Isotope number densities of the outer core fissile fuel

Isotope	Number density, $\times 10^{24}$ cm^{-3}			
	"20°C"	"180°C"	"HZP"	"HFP"
U-235	9.71287E-05	9.69769E-05	9.67661E-05	9.65435E-05
U-238	1.90845E-02	1.90547E-02	1.90132E-02	1.89695E-02
Pu-238	2.21382E-05	2.21036E-05	2.20555E-05	2.20048E-05
Pu-239	3.05349E-03	3.04872E-03	3.04209E-03	3.03509E-03
Pu-240	9.10417E-04	9.08994E-04	9.07018E-04	9.04932E-04
Pu-241	2.44768E-04	2.44385E-04	2.43854E-04	2.43293E-04
Pu-242	8.49515E-05	8.48187E-05	8.46343E-05	8.44396E-05
Am-241	5.99070E-05	5.98134E-05	5.96833E-05	5.95460E-05
O	4.66433E-02	4.65704E-02	4.64692E-02	4.63623E-02

Table 7. Isotope number densities of the fertile fuel

Isotope	Number density, $\times 10^{24}$ cm^{-3}			
	"20°C"	"180°C"	"HZP"	"HFP"
U-235	5.92251E-05	5.91325E-05	5.90040E-05	5.88683E-05
U-238	2.33323E-02	2.32958E-02	2.32452E-02	2.31917E-02
O	4.63152E-02	4.62428E-02	4.61423E-02	4.60361E-02

Table 8. Isotope number densities of 316Ti construction steel

Isotope	Number density, $\times 10^{24}$ cm^{-3}			
	"20°C"	"180°C"	"HZP"	"HFP"
C_{nat}	1.99483E-04	1.97913E-04	1.95513E-04	1.95513E-04
Si-28	9.46910E-04	9.39458E-04	9.28063E-04	9.28063E-04
Si-29	4.64444E-05	4.60789E-05	4.55200E-05	4.55200E-05
Si-30	2.96324E-05	2.93992E-05	2.90426E-05	2.90426E-05
P-31	4.63709E-05	4.60060E-05	4.54479E-05	4.54479E-05
Ti-46	3.43812E-05	3.41106E-05	3.36969E-05	3.36969E-05
Ti-47	3.03458E-05	3.01070E-05	2.97418E-05	2.97418E-05
Ti-48	2.94438E-04	2.92121E-04	2.88578E-04	2.88578E-04
Ti-49	2.11661E-05	2.09995E-05	2.07448E-05	2.07448E-05
Ti-50	1.98618E-05	1.97055E-05	1.94665E-05	1.94665E-05
Cr-50	6.66387E-04	6.61142E-04	6.53123E-04	6.53123E-04
Cr-52	1.23572E-02	1.22599E-02	1.21112E-02	1.21112E-02
Cr-53	1.37473E-03	1.36391E-03	1.34737E-03	1.34737E-03
Cr-54	3.35867E-04	3.33224E-04	3.29182E-04	3.29182E-04
Mn-55	1.48147E-03	1.46981E-03	1.45198E-03	1.45198E-03
Fe-54	3.35763E-03	3.33120E-03	3.29080E-03	3.29080E-03
Fe-56	5.08275E-02	5.04275E-02	4.98158E-02	4.98158E-02
Fe-57	1.15320E-03	1.14412E-03	1.13025E-03	1.13025E-03
Fe-58	1.50826E-04	1.49639E-04	1.47824E-04	1.47824E-04
Ni-58	7.87595E-03	7.81396E-03	7.71919E-03	7.71919E-03
Ni-60	2.93277E-03	2.90969E-03	2.87440E-03	2.87440E-03
Ni-61	1.25393E-04	1.24406E-04	1.22897E-04	1.22897E-04
Ni-62	3.93381E-04	3.90285E-04	3.85551E-04	3.85551E-04
Ni-64	9.70357E-05	9.62720E-05	9.51043E-05	9.51043E-05
Mo-92	1.89224E-04	1.87735E-04	1.85458E-04	1.85458E-04
Mo-94	1.16625E-04	1.15707E-04	1.14304E-04	1.14304E-04
Mo-95	1.99765E-04	1.98193E-04	1.95789E-04	1.95789E-04
Mo-96	2.08043E-04	2.06406E-04	2.03902E-04	2.03902E-04
Mo-97	1.18571E-04	1.17638E-04	1.16211E-04	1.16211E-04
Mo-98	2.98169E-04	2.95822E-04	2.92234E-04	2.92234E-04
Mo-100	1.17644E-04	1.16718E-04	1.15302E-04	1.15302E-04

Table 9. Isotope number densities of the diluent subassembly homogenized composition

Isotope	Number density, $\times 10^{24}$ cm^{-3}			
	"20°C"	"180°C"	"HZP"	"HFP"
Si-28	6.22000E-04	6.17212E-04	6.09818E-04	6.09818E-04
Si-29	3.15000E-05	3.12575E-05	3.08830E-05	3.08830E-05
Si-30	2.09000E-05	2.07391E-05	2.04907E-05	2.04907E-05
Ti-46	2.30000E-05	2.28229E-05	2.25495E-05	2.25495E-05
Ti-47	2.10000E-05	2.08383E-05	2.05887E-05	2.05887E-05
Ti-48	2.12000E-04	2.10368E-04	2.07848E-04	2.07848E-04
Ti-49	1.58000E-05	1.56784E-05	1.54905E-05	1.54905E-05
Ti-50	1.55000E-05	1.53807E-05	1.51964E-05	1.51964E-05
Cr-50	2.19418E-04	2.17729E-04	2.15120E-04	2.15120E-04
Cr-52	4.23704E-03	4.20442E-03	4.15405E-03	4.15405E-03
Cr-53	4.80447E-04	4.76748E-04	4.71037E-04	4.71037E-04
Cr-54	1.19593E-04	1.18672E-04	1.17251E-04	1.17251E-04
Mn-55	9.40570E-04	9.33329E-04	9.22148E-04	9.22148E-04
Fe-54	1.01918E-03	1.01133E-03	9.99218E-04	9.99218E-04
Fe-56	1.61170E-02	1.59929E-02	1.58013E-02	1.58013E-02
Fe-57	3.86584E-04	3.83608E-04	3.79012E-04	3.79012E-04
Fe-58	4.92016E-05	4.88228E-05	4.82379E-05	4.82379E-05
Ni-58	2.51082E-03	2.49149E-03	2.46164E-03	2.46164E-03
Ni-60	9.64157E-04	9.56735E-04	9.45273E-04	9.45273E-04
Ni-61	4.20455E-06	4.17218E-06	4.12220E-06	4.12220E-06
Ni-62	1.34029E-04	1.32997E-04	1.31404E-04	1.31404E-04
Ni-64	3.41527E-05	3.38898E-05	3.34838E-05	3.34838E-05
Mo-92	6.57917E-05	6.52852E-05	6.45031E-05	6.45031E-05
Mo-94	4.10090E-05	4.06933E-05	4.02058E-05	4.02058E-05
Mo-95	7.05797E-05	7.00364E-05	6.91973E-05	6.91973E-05
Mo-96	7.39491E-05	7.33798E-05	7.25007E-05	7.25007E-05
Mo-97	4.23390E-05	4.20131E-05	4.15097E-05	4.15097E-05
Mo-98	1.06978E-04	1.06154E-04	1.04883E-04	1.04883E-04
Mo-100	4.26936E-05	4.23649E-05	4.18574E-05	4.18574E-05
Cu-63	1.31000E-04	1.29992E-04	1.28434E-04	1.28434E-04
Cu-65	5.85000E-05	5.80497E-05	5.73542E-05	5.73542E-05
Na-23	5.76350E-03	5.71913E-03	5.65062E-03	5.65062E-03

Table 10. Isotope number densities of the radial shielding subassembly homogenized composition

Isotope	Number density, $\times 10^{24}$ cm^{-3}			
	"20°C"	"180°C"	"HZP"	"HFP"
Si-28	4.23000E-04	4.19744E-04	4.14715E-04	4.14715E-04
Si-29	2.14000E-05	2.12353E-05	2.09809E-05	2.09809E-05
Si-30	1.42000E-05	1.40907E-05	1.39219E-05	1.39219E-05
Ti-46	1.57000E-05	1.55791E-05	1.53925E-05	1.53925E-05
Ti-47	1.43000E-05	1.41899E-05	1.40199E-05	1.40199E-05
Ti-48	1.44000E-04	1.42891E-04	1.41180E-04	1.41180E-04
Ti-49	1.08000E-05	1.07169E-05	1.05885E-05	1.05885E-05
Ti-50	1.06000E-05	1.05184E-05	1.03924E-05	1.03924E-05
Cr-50	3.32910E-04	3.30347E-04	3.26390E-04	3.26390E-04
Cr-52	6.41983E-03	6.37041E-03	6.29409E-03	6.29409E-03
Cr-53	7.27957E-04	7.22353E-04	7.13699E-04	7.13699E-04
Cr-54	1.81204E-04	1.79809E-04	1.77655E-04	1.77655E-04
Mn-55	6.39840E-04	6.34914E-04	6.27308E-04	6.27308E-04
Fe-54	1.54425E-03	1.53236E-03	1.51400E-03	1.51400E-03
Fe-56	2.44205E-02	2.42325E-02	2.39422E-02	2.39422E-02
Fe-57	5.85750E-04	5.81241E-04	5.74278E-04	5.74278E-04
Fe-58	7.45500E-05	7.39761E-05	7.30899E-05	7.30899E-05
Ni-58	3.80428E-03	3.77499E-03	3.72977E-03	3.72977E-03
Ni-60	1.46539E-03	1.45411E-03	1.43669E-03	1.43669E-03
Ni-61	6.37055E-06	6.32151E-06	6.24578E-06	6.24578E-06
Ni-62	2.03075E-04	2.01512E-04	1.99098E-04	1.99098E-04
Ni-64	5.17467E-05	5.13483E-05	5.07332E-05	5.07332E-05
Mo-92	9.96832E-05	9.89158E-05	9.77308E-05	9.77308E-05
Mo-94	6.21341E-05	6.16558E-05	6.09171E-05	6.09171E-05
Mo-95	1.06938E-04	1.06115E-04	1.04844E-04	1.04844E-04
Mo-96	1.12043E-04	1.11180E-04	1.09849E-04	1.09849E-04
Mo-97	6.41493E-05	6.36555E-05	6.28929E-05	6.28929E-05
Mo-98	1.62086E-04	1.60838E-04	1.58911E-04	1.58911E-04
Mo-100	6.46866E-05	6.41886E-05	6.34196E-05	6.34196E-05
Cu-63	8.93000E-05	8.86126E-05	8.75510E-05	8.75510E-05
Cu-65	3.98000E-05	3.94936E-05	3.90205E-05	3.90205E-05
Na-23	1.09310E-02	1.08469E-02	1.07169E-02	1.07169E-02

Table 11. Isotope number densities of boron carbide

Isotope	Number density, $\times 10^{24}$ cm^{-3}			
	"20°C"	"180°C"	"HZP"	"HFP"
C_{nat}	2.46696E-02	2.46499E-02	2.46228E-02	2.46228E-02
B-10	8.88105E-02	8.87395E-02	8.86421E-02	8.86421E-02
B-11	9.86783E-03	9.85994E-03	9.84912E-03	9.84912E-03

Table 12. Number density of sodium

Isotope	Number density, $\times 10^{24}$ cm^{-3}		
	"180°C"	"HZP"	"HFP"
Na-23	2.37718e-02	2.24691e-02	2.24691e-02

Table 13. Core thermal configurations

Core configuration	Temperature for geometry calculation, K			
	Fissile fuel	Fertile fuel	Sodium	Structure steel/ absorber
“20°C”	293	293	453	293
“180°C”	453	453	453	453
“HZP” (400°C)	673	673	673	673
“HFP”	1500	900	673	673

Table 14. Core configurations for benchmark criticality calculations

Criticality case ID_{Crit}	CSD insertion*, cm	Temperature for XS/geometry, K		
		Fissile	Fertile	Other
1	0	300/293	300/293	300/293
2	0	300/453	300/453	300/453
3	0	453/453	453/453	453/453
4	100	453/453	453/453	453/453
5	0	300/673	300/673	300/673
6	40	300/673	300/673	300/673
7	0	600/673	600/673	600/673
8	40	600/673	600/673	600/673
9	0	600/673	600/673	300/673
10	0	673/673	673/673	673/673
11	40	673/673	673/673	673/673
12	0	900/673	900/673	900/673
13	0	1500/1500	900/900	600/673

(*) From the top of fissile pellet stack

Table 15. Doppler constant definitions

Doppler constant case $ID_{Doppler}$	Description
1	300K – 600K, all isotopes, CRs withdrawn (ID_{Crit} 5–7)
2	300K – 900K, all isotopes, CRs withdrawn (ID_{Crit} 5–12)
3	300K – 600K, fissile/fertile zone isotopes only, CRs withdrawn (ID_{Crit} 5–9)
4	300K – 600K, all isotopes, CRs inserted by 40 cm (ID_{Crit} 6–8)

Table 16. Isothermal expansion coefficient

Expansion coefficient ID_{Exp}	Description
1	Isothermal temperature coefficient 400℃-180℃ (ID_{Crit} 10–3)
2	Isothermal temperature coefficient 400℃-180℃ as sum of components (ID_{Crit} 5–2 for geometry expansion and ID_{Crit} 5–7 for Doppler constant)
3	Isothermal temperature coefficient 400℃-180℃ as sum of components (ID_{Crit} 5–2 for geometry expansion and ID_{Crit} 6–8 for Doppler constant)
4	Expansion component *k* (ID_{Crit} 5–2)

Table 17. Multiplication factor values for different core configurations obtained with Reference solution. Standard deviation for multiplication factor is less than 1 pcm in all cases

ID_{Crit}	Multiplication factor, unitless
1	1.04365
2	1.04246
3	1.03670
4	0.95119
5	1.04080
6	1.00824
7	1.03053
8	0.99894
9	1.03139
10	1.02886
11	0.99742
12	1.02483
13	1.01903

Table 18. CR worth curve obtained with Reference solution

CSD insertion*, %	Reactivity change, pcm
-10	183
0	0
10	-397
20	-1048
30	-1953
40	-3069
50	-4381
60	-5717
70	-6930
80	-7856
90	-8433
100	-8701
110	-8794
*) percentage of fissile height	

Table 19. Reactivity characteristics obtained with Reference solution

Description		Value
Fuel Doppler constant, pcm		
1	IC fissile	-757
2	OC fissile	-257
3	RB	-28
4	LAB	-54
5	UAB	-19
6	Total	-1135
Sodium density effect, pcm/K		
1	IC total height	0.170
2	OC total height	0.011
3	RB total height	-0.010
4	IC fissile	0.188
5	OC fissile	0.019
6	IC+OC fissile	0.206
Sodium Void Effect, pcm		
1	IC SVE fissile	770
2	OC SVE fissile	83
3	IC SVE fissile + no CRs	885
4	OC SVE fissile + no CRs	83
Fuel axial expansion effect, pcm/K		
1	IC fissile + fertile	-0.108
2	OC fissile + fertile	-0.084
3	IC+OC+RB Fiss+Fert	-0.186
Clad expansion effect, pcm/K		
1	IC fertile + fissile	0.118
2	OC fertile + fissile	0.026
3	IC fertile + fissile Doppler (+490C)	0.056
4	OC fertile + fissile Doppler (+490C)	0.000
Hexcan expansion effect, pcm/K		
1	IC fertile + fissile	0.050
2	OC fertile + fissile	0.014
3	IC fertile + fissile Doppler (+490C)	-0.001
4	OC fertile + fissile Doppler (+490C)	-0.002
Diagrid expansion effect, pcm/K		-0.992

Table 20. Subassembly power value in MW obtained with Reference solution. The SA numbers are defined in accord to core map of Figure 1 (see also Figure 17) from left to right, from top to bottom for all fuel (non-zero power) subassemblies

1	9118	41	64685	81	66246	121	345601	161	5666460	201	9284900	241	8891500	281	17669
2	8435	42	29547	82	202352	122	5464510	162	345722	202	9421840	242	8764130	282	64520
3	8382	43	26742	83	457946	123	7501000	163	80599	203	10038100	243	8763300	283	310471
4	8874	44	53336	84	5463050	124	8437370	164	23819	204	10098300	244	8891570	284	5645380
5	22663	45	115533	85	7193960	125	9239960	165	64507	205	9574900	245	9587650	285	8130050
6	25674	46	322174	86	8274500	126	8304670	166	302072	206	8621180	246	10093900	286	9040700
7	26958	47	4287400	87	8563930	127	8316460	167	5377290	207	8724400	247	10135500	287	8252580
8	26997	48	5310400	88	8936930	128	8600920	168	7900320	208	7502660	248	9476360	288	9552430
9	26964	49	5820450	89	9273410	129	9054220	169	9113140	209	4742310	249	8323500	289	10095200
10	26455	50	5975840	90	8875100	130	8707650	170	8341710	210	202619	250	9239830	290	9416870
11	25929	51	5942640	91	9008060	131	8688310	171	9473450	211	43747	251	8236890	291	8761260
12	24369	52	5908190	92	8258210	132	8963560	172	10054100	212	25607	252	5464910	292	9300950
13	21541	53	5773760	93	8136680	133	8478450	173	10154000	213	93606	253	243055	293	9454880
14	18435	54	5465720	94	6926250	134	8259980	174	10072500	214	436171	254	53354	294	9300740
15	35721	55	5006800	95	5183000	135	8106830	175	10091500	215	6370460	255	29521	295	8766180
16	60456	56	4105400	96	436748	136	8064970	176	10076400	216	8060400	256	110867	296	9450470
17	78883	57	310337	97	195378	137	7294340	177	10034200	217	8269850	257	490357	297	10157200
18	89048	58	110969	98	64590	138	5378160	178	10103300	218	9567180	258	6920590	298	9633720
19	93037	59	50984	99	23365	139	343004	179	9985400	219	10088000	259	8825460	299	8317540
20	93702	60	25647	100	25193	140	84908	180	9379890	220	9285620	260	8098000	300	8275530
21	92796	61	43847	101	80680	141	25204	181	8276790	221	8828030	261	9133530	301	5829460
22	90116	62	97772	102	308902	142	23333	182	9284450	222	8822150	262	9975500	302	322246
23	84595	63	242893	103	4741190	143	79417	183	9114680	223	9275150	263	10031500	303	67303
24	74621	64	511096	104	6706400	144	343117	184	7951060	224	10081200	264	9268260	304	18423
25	57539	65	5827510	105	8236120	145	5666010	185	5464730	225	9585670	265	8885220	305	34143
26	34155	66	7157320	106	9128060	146	7951750	186	308970	226	8342000	266	9113680	306	166942
27	17692	67	7871270	107	7979980	147	8725810	187	66338	227	8437500	267	9301060	307	4101240
28	30821	68	8233460	108	7952060	148	8323590	188	42202	228	6709240	268	9299500	308	6866060
29	67259	69	8156540	109	7909570	149	9268960	189	195261	229	458403	269	9116090	309	8250580
30	174438	70	8058030	110	7733230	150	9633330	190	4580590	230	97936	270	8894610	310	8471660
31	291092	71	8075380	111	9052110	151	9864970	191	7292310	231	26739	271	9289790	311	9787340
32	346579	72	7766690	112	8833110	152	9899180	192	8577950	232	50901	272	10075500	312	10027700
33	369805	73	7363640	113	7757370	153	9825090	193	9277750	233	231255	273	10057600	313	9280660
34	374808	74	6873190	114	6373010	154	9859220	194	8618740	234	5179030	274	9267870	314	8823560
35	372986	75	5650890	115	4582730	155	9793820	195	9582340	235	7750480	275	8303140	315	9302030
36	367474	76	491002	116	302112	156	9559520	196	10131700	236	8063410	276	9130420	316	9299680
37	352379	77	231282	117	79543	157	9142630	197	10073600	237	9372340	277	7196480	317	8828160
38	326306	78	93615	118	25040	158	8069320	198	9448980	238	10089300	278	511097	318	9298980
39	276175	79	42232	119	25038	159	8582710	199	9299230	239	10074200	279	115668	319	10072400
40	167120	80	23825	120	84890	160	7900350	200	9591480	240	9581630	280	30808	320	9866420

321	8601790	361	9298990	401	8046950	441	93629	481	7356020	521	276223	561	202281
322	8564580	362	8889230	402	7945440	442	26971	482	5461320	522	74666	562	308779
323	7159910	363	8885720	403	9049180	443	9129	483	352147	523	24412	563	345292
324	4288860	364	9283360	404	9859260	444	8352	484	90049	524	22636	564	342822
325	174748	365	10076100	405	10153500	445	26913	485	26461	525	60292	565	301675
326	35686	366	9824250	406	10069800	446	93605	486	8339	526	174342	566	195193
327	57437	367	8705450	407	10085200	447	374319	487	9103	527	322110	567	93533
328	275995	368	7947780	408	10068800	448	5969410	488	26960	528	510708	568	50951
329	5001770	369	9271110	409	10026100	449	8224830	489	89014	529	5461100	569	29453
330	7357250	370	8229970	410	10092300	450	8929270	490	346318	530	6704570	570	17664
331	7725480	371	5821220	411	9789480	451	8311500	491	5305950	531	7497150	571	26718
332	8955260	372	346737	412	8959590	452	9263060	492	7152640	532	7944330	572	43792
333	9856150	373	78905	413	7906620	453	9466680	493	8269360	533	7891140	573	66232
334	10076600	374	22720	414	8868510	454	9573540	494	9123280	534	7285230	574	80624
335	9592850	375	24399	415	8053120	455	9559740	495	9235100	535	6365650	575	84743
336	8827470	376	84438	416	5939750	456	9365320	496	9269220	536	5177110	576	79478
337	8763420	377	352037	417	374354	457	9129990	497	8820860	537	490547	577	64442
338	9114690	378	5765310	418	93004	458	8251810	498	8128050	538	310235	578	42214
339	8760350	379	8063290	419	26942	459	7759190	499	6863320	539	166995	579	25635
340	8822570	380	8864520	420	8858	460	5769280	500	5002260	540	57458	580	23785
341	9591310	381	8703800	421	26458	461	367217	501	326083	541	21532	581	25187
342	10092900	382	9896780	422	92803	462	92676	502	84666	542	35701	582	25006
343	9899590	383	10068000	423	372436	463	26928	503	25916	543	67309	583	23312
344	9051990	384	9447290	424	5936190	464	8453	504	8863	544	115617	-	-
345	7977960	385	9283550	425	8148310	465	8443	505	25633	545	242793	-	-
346	8935800	386	9575850	426	9265870	466	26972	506	78753	546	458040	-	-
347	7873490	387	9264710	427	7973450	467	93005	507	290984	547	4739150	-	-
348	5311750	388	9414050	428	8594800	468	369687	508	4283810	548	5459860	-	-
349	291348	389	10027100	429	9628340	469	5816520	509	5823560	549	5661610	-	-
350	60415	390	9856830	430	10050200	470	7865960	510	7190170	550	5372850	-	-
351	21502	391	8687030	431	10123300	471	8557430	511	8231660	551	4576600	-	-
352	74566	392	8152520	432	10084900	472	8298770	512	8431400	552	436045	-	-
353	325811	393	5971860	433	9973680	473	8316500	513	8717870	553	230900	-	-
354	5459900	394	369560	434	9550410	474	8332010	514	9102370	554	110897	-	-
355	7758410	395	89036	435	8475570	475	8610200	515	8570250	555	64512	-	-
356	8998070	396	25685	436	7729130	476	8263410	516	8052880	556	34111	-	-
357	7901950	397	25881	437	9002290	477	8057420	517	7746840	557	18419	-	-
358	8684520	398	89924	438	8067650	478	8093770	518	6919020	558	30840	-	-
359	9822670	399	366623	439	5905610	479	9040190	519	5643700	559	53337	-	-
360	10090100	400	5901640	440	372684	480	8251120	520	4101110	560	97832	-	-

Table 21. Axial power profiles obtained with Reference solution

	Axial position (from bottom of LAB), cm			Normalized power		
Layer	From	To	Midpoint	IC	OC	RB
1	0.000	10.037	5.019	0.039	0.023	0.006
2	10.037	20.075	15.056	0.068	0.043	0.009
3	20.075	30.112	25.094	0.150	0.100	0.016
4	30.112	40.150	35.131	2.229	1.702	0.026
5	40.150	50.187	45.169	2.848	2.198	0.036
6	50.187	60.225	55.206	3.334	2.587	0.044
7	60.225	70.262	65.244	3.614	2.814	0.048
8	70.262	80.300	75.281	3.655	2.857	0.050
9	80.300	90.337	85.319	3.457	2.716	0.048
10	90.337	100.375	95.356	3.065	2.425	0.044
11	100.375	110.412	105.393	2.578	2.048	0.038
12	110.412	120.450	115.431	2.045	1.624	0.031
13	120.450	130.487	125.468	1.499	1.181	0.022
14	130.487	140.525	135.506	0.099	0.068	0.013
15	140.525	150.562	145.543	0.042	0.027	0.007
16	150.562	160.600	155.581	0.021	0.013	0.005

Table 22. Reference solution for axial distribution of U-235 fission reaction rate

Point number	Axial position *, cm	Normalized rate	Point number	Axial position *, cm	Normalized rate	Point number	Axial position *, cm	Normalized rate	Point number	Axial position *, cm	Normalized rate
1	0.803	0.3481	26	40.953	0.7414	51	81.103	0.9547	76	121.253	0.4293
2	2.409	0.3436	27	42.559	0.7645	52	82.709	0.9395	77	122.859	0.4101
3	4.015	0.3470	28	44.165	0.7877	53	84.315	0.9231	78	124.465	0.3912
4	5.621	0.3547	29	45.771	0.8104	54	85.921	0.9053	79	126.071	0.3737
5	7.227	0.3647	30	47.377	0.8329	55	87.527	0.8855	80	127.677	0.3570
6	8.833	0.3785	31	48.983	0.8534	56	89.133	0.8643	81	129.283	0.3430
7	10.439	0.3927	32	50.589	0.8733	57	90.739	0.8418	82	130.889	0.3319
8	12.045	0.4089	33	52.195	0.8921	58	92.345	0.8185	83	132.495	0.3203
9	13.651	0.4274	34	53.801	0.9095	59	93.951	0.7943	84	134.101	0.3069
10	15.257	0.4470	35	55.407	0.9257	60	95.557	0.7711	85	135.707	0.2928
11	16.863	0.4677	36	57.013	0.9404	61	97.163	0.7479	86	137.313	0.2784
12	18.469	0.4883	37	58.619	0.9537	62	98.769	0.7252	87	138.919	0.2640
13	20.075	0.5090	38	60.225	0.9653	63	100.375	0.7031	88	140.525	0.2494
14	21.681	0.5299	39	61.831	0.9753	64	101.981	0.6815	89	142.131	0.2352
15	23.287	0.5499	40	63.437	0.9843	65	103.587	0.6597	90	143.737	0.2213
16	24.893	0.5687	41	65.043	0.9905	66	105.193	0.6382	91	145.343	0.2075
17	26.499	0.5858	42	66.649	0.9959	67	106.799	0.6168	92	146.949	0.1953
18	28.105	0.5999	43	68.255	0.9986	68	108.405	0.5958	93	148.555	0.1834
19	29.711	0.6098	44	69.861	1.0000	69	110.011	0.5744	94	150.161	0.1722
20	31.317	0.6176	45	71.467	0.9990	70	111.617	0.5532	95	151.767	0.1624
21	32.923	0.6321	46	73.073	0.9965	71	113.223	0.5319	96	153.373	0.1527
22	34.529	0.6511	47	74.679	0.9919	72	114.829	0.5109	97	154.979	0.1454
23	36.135	0.6724	48	76.285	0.9853	73	116.435	0.4902	98	156.585	0.1390
24	37.741	0.6943	49	77.891	0.9770	74	118.041	0.4697	99	158.191	0.1343
25	39.347	0.7180	50	79.497	0.9667	75	119.647	0.4491	100	159.797	0.1322

* from bottom of LAB

Table 23. Reference solution for U-238 and Pu-239 fission rate ratio

SA row number	^{238}U fission rate ratio	^{239}Pu fission rate ratio
1	0.847	0.969
2	0.717	0.757
3	-	-
4	0.847	0.783
5	1.000	1.000
6	0.939	0.933
7	0.722	0.721
8	-	-
9	0.733	0.658
10	0.526	0.482
11	0.105	0.255

Table 24. Reference solution for kinetics parameters

Prompt neutron lifetime, s	4.939E-07							
Effective delayed neutrons fraction, pcm	3.707E+02							
Group number	1	2	3	4	5	6	7	8
Group effective delayed neutrons fraction, pcm	6.165E+00	6.057E+01	2.251E+01	5.413E+01	1.170E+02	4.779E+01	4.197E+01	2.056E+01
Group decay constant, s^{-1}	1.247E-02	2.829E-02	4.252E-02	1.330E-01	2.925E-01	6.665E-01	1.635E+00	3.555E+00

Table 25. Criticality of selected core configurations

Solution	Multiplication factor value and difference from Reference, pcm				
	1 “20°C”	3 “180°C”	7 $Conf_1$	10 “HZP”	13 “HFP”
Serpent| JEFF311 (Reference)	1.03670	1.01903	1.03053	1.00824	0.95119
SCALE623/KENO-VI	1.03725	1.02008	1.03158	1.00869	0.95107
|ENDFB71	55	105	105	45	-12
MCNP611b|	1.03707	1.01970	1.03112	1.00914	0.95152
JEFF311	37	67	59	90	33
WIMS/MONK|	1.03830	1.02030	1.03260	1.00900	0.94720
JEFF311	160	127	207	76	-399
Serpent/DYN3D|	1.03607	1.01809	1.02978	1.00749	0.95035
JEF311	-63	-94	-75	-75	-84
WIMS/SP3|	1.03804	1.01834	1.03230	1.00915	0.94890
JEFF311	134	-69	177	91	-229
Serpent/PARCS|	1.03647	1.01781	1.03019	1.00666	0.94660
JEFF311	-23	-122	-34	-158	-459
DRAGON/DONJON|	1.01273	0.99609	1.00783	0.98347	0.92324
JEFF311	-2397	-2294	-2270	-2477	-2795

Table 26. Kinetic parameters

Parameter	Serpent| JEFF311 (Reference)	MCNP611b| JEFF311	Serpent/DYN3D| JEF311	WIMS/SP3| JEFF311
Prompt neutron lifetime, s	4.939E-07	4.925E-07	9.4321E-07	3.422E-07
Effective delayed neutrons fraction, pcm	370.7	369.0	365.5	369.6

Table 27. Evaluated discrepancies of selected predicted parameters

Parameter	Monte Carlo		Deterministic	
	All results	One outlier value removed	All results	One outlier value removed
Multiplication factor (no CRs inserted)	230 pcm	-	340 pcm	-
CRs worth (100% insertion)	732 pcm (8%)	77 pcm (0.9%)	529 pcm (6%)	434 pcm (5%)
Fuel Doppler constant	82 pcm (7%)	21 pcm (1.9%)	37 pcm (3.2%)	19 pcm (1.7%)
"Cold" fuel Doppler constant	95 pcm (8%)	47 pcm (3.7%)	169 pcm (13%)	61 pcm (4.8%)
Sodium density coefficient	0.009 pcm/K (4.4%)	-	0.064 pcm/K (31%)	-
SVE (with 40 cm inserted CRs)	185 pcm (22%)	33 pcm (3.9%)	311 pcm (37%)	184 pcm (22%)
SVE (no CRs inserted)	294 pcm (30%)	31 pcm (3.2%)	694 pcm (72%)	479 pcm (50%)
Axial fuel expansion coefficient	0.046 pcm/K (25%)	0.031 pcm/K (17%)	0.17 pcm/K (90%)	0.08 pcm/K (43%)
Diagrid expansion coefficient	0.18 pcm/K (18%)	0.013 pcm/K (7%)	0.43 pcm/K (43%)	0.18 pcm/K (18%)